ADVANCED MATERIALS

In article number 2212315, Guomin Wang, Kaiwei Tang, Jianzhong Du, Paul K. Chu, and co-workers report a titanium nitride nanowire coating synthesized by a liquid-phase oxidation process and nitridation. The charged surfaces kill bacteria by exerting electro–mechanical forces, piercing the bacterial membrane and disturbing the electron balance. This work provides new insights into the design of high-performance antibacterial interfaces with clinical applications.

WILEY VCH

ANTIBACTERIAL SURFACES

Check for updates

ADVANCED MATERIALS
www.advmat.de

Quantifiable Relationship Between Antibacterial Efficacy and Electro–Mechanical Intervention on Nanowire Arrays

Guomin Wang, Kaiwei Tang,* Wenjuan Jiang, Qing Liao, Yong Li, Pei Liu, Yuzheng Wu, Mengting Liu, Huaiyu Wang, Bin Li, Jianzhong Du,* and Paul K. Chu**

Physical disruption is an important antibacterial means as it is lethal to bacteria without spurring antimicrobial resistance. However, it is very challenging to establish a quantifiable relationship between antibacterial efficacy and physical interactions such as mechanical and electrical forces. Herein, titanium nitride (TN) nanowires with adjustable orientations and capacitances are prepared to exert gradient electro–mechanical forces on bacteria. While vertical nanowires show the strongest mechanical force resulting in an antibacterial efficiency of 0.62 log reduction (vs 0.22 for tiled and 0.36 for inclined nanowires, respectively), the addition of electrical charges maximizes the electro–mechanical interactions and elevates the antibacterial efficacy to more than 3 log reduction. Biophysical and biochemical analyses indicate that electrostatic attraction by electrical charge narrows the interface. The electro–mechanical intervention more easily stiffens and rips the bacteria membrane, disturbing the electron balance and generating intracellular oxidative stress. The antibacterial ability is maintained in vivo and bacteria-challenged rats are protected from serious infection. The physical bacteria-killing process demonstrated here can be controlled by adjusting the electro–mechanical interactions. Overall, these results revealed important principles for rationally designing high-performance antibacterial interfaces for clinical applications.

1. Introduction

Non-leaching antibacterial implant materials can cope with bacterial infection after surgery. Compared to conventional leaching surfaces based on antibiotics or other agents release, there are very few systemic side effects and drug resistance.[1] Besides, there is no need to replenish the antibacterial agents which can be toxic in high quantities.[2,3] Non-leaching bactericidal surfaces are usually based on physical processes such as mechanical forces,[4,5] electrical interactions,[6] and thermal stimuli.[7] For instance, the sharp edges on surfaces can induce membrane stress in bacteria upon contact, resulting in membrane collapse and eventual death.[8,9] It has been observed that bacteria falling between nanostructures in cicada wings gradually lose viability.[10] Inspired by nature, nanopillars with high aspect ratios have been designed on black silicon,[11] graphene,[12]

G. Wang, J. Du
Department of Orthopedics
Shanghai Tenth People's Hospital
School of Medicine
Tongji University
Shanghai 200072, P. R. China
E-mail: gwang@tongji.edu.cn; jzdu@tongji.edu.cn

G. Wang, K. Tang, P. Liu, Y. Wu, P. K. Chu
Department of Physics
Department of Materials Science and Engineering and Department of Biomedical Engineering
City University of Hong Kong
Tat Chee Avenue, Kowloon, Hong Kong 999077, P. R. China
E-mail: paul.chu@cityu.edu.hk

K. Tang
School of Materials Science and Engineering
Xiangtan University
Xiangtan, Hunan 411105, P. R. China
E-mail: tangkaiwei@xtu.edu.cn

W. Jiang
College of Pharmacy
Western University of Health Sciences
309 E. Second St, Pomona, CA 91766, USA

The ORCID identification number(s) for the author(s) of this article can be found under https://doi.org/10.1002/adma.202212315.

DOI: 10.1002/adma.202212315

Q. Liao, H. Wang
Center for Human Tissues and Organs Degeneration
Shenzhen Institutes of Advanced Technology
Chinese Academy of Sciences
Shenzhen 518055, P. R. China

Y. Li
Department of Applied Biology and Chemical Technology and the State Key Laboratory of Chemical Biology and Drug Discovery
The Hong Kong Polytechnic University
Hung Hom, Kowloon, Hong Kong 999077, P. R. China

M. Liu
USC Stevens Neuroimaging and Informatics Institute
Keck School of Medicine of USC
University of Southern California
Los Angeles, CA 90033, USA

B. Li
Department of Orthopaedic Surgery
Orthopaedic Institute
First Affiliated Hospital
Medical College
Soochow University
Suzhou, Jiangsu 215007, P. R. China

J. Du
Department of Polymeric Materials
School of Materials Science and Engineering
Tongji University
4800 Caoan Road, Shanghai 201804, P. R. China

 © 2023 Wiley-VCH GmbH

or other flexible substrate[13] to achieve tailorable antibacterial efficiency. There is direct evidence that deformation and subsequent penetration of the bacterial envelope are responsible for bacterial death.[14]

Extracellular electron transfer (EET) is another means to eliminate bacteria.[15] Electron transfer takes place both on non-insulators and in the respiratory chain of micro-organisms producing electron exchange as a result of the potential difference at the bacteria-materials interface.[16] In our previous study, an antibacterial platform based on positively charged capacitive coatings was demonstrated to exhibit antibacterial effects[17] and instantaneous electron transfer between charged capacitive materials and bacteria was observed. Subsequently, Panda et al. observed a similar phenomenon.[18] This work paved a new way for antibacterial implants, however, in-depth investigation of the mechanism or a quantifiable relationship between the antibacterial efficacy and physical forces has hitherto not been reported. In addition, antibacterial efficiency is another critical factor determining the clinical practicality of implants. Several research groups have fabricated nanostructures with antibacterial efficiency of 80%,[14,19] implying that the bacterial population can be reduced from 5 million to 1 million, but if the remaining bacteria were left alone for 40 min, millions of bacteria can regrow causing serious infection. Hence, a more effective surface that can kill more bacteria by simply tuning the physical stress is highly desirable in preventing infection.

Although bacteria can resist surface tension created by the flow of saliva or blood (up to 10 dynes cm^{-2}),[20] a sufficiently large contact stress can destroy the bacteria or even kill them.[11,21,22] However, it is difficult to control the antibacterial effects based on such passive contact between the bacteria and the surface.[8,23] Nonetheless, the electrostatic interactions on a positively charged surface can supplement the mechanical forces to kill bacteria. In fact, electron transfer at the interface can alone disrupt the metabolism of bacteria.[24] Hence, a charged capacitive surface with the desirable micro–nano structure is expected to eliminate bacteria more effectively by electro–mechanical intervention than by a single strategy. Beyond that, it is important to derive a quantitative relationship between these parameters and bacteria-killing efficacy and elucidate the underlying mechanism in order to exploit a controllable antibacterial surface and obtain a universal biophysical strategy for future antibacterial materials design.

In this work, capacitive titanium nitride nanowires (TN) with an adjustable topography are designed and prepared to exert gradient mechanical and/or electrical stress on bacteria. Progressively increasing antibacterial efficiency against bacteria is observed when the surface morphology is changed from tiled nanowires to vertical ones and the charged capacitive vertical nanowires enhance the antibacterial efficiency significantly. Experiments and theoretical simulations are carried out to quantitatively reveal how the electro–mechanical interaction leads to not only violent piercing, but also disturbance of the membrane potentials and electron balance. The dual effects produce large surface tension on the bacterial membrane as well as reactive oxygen species (ROS) bursts in the bacteria, which rescue rats from bacterial infection in vivo.

2. Results

Titanium oxide (TO) nanowires with different densities and orientations were fabricated on titanium by a facile chemical dissolution-nucleation technique and the morphological changes are shown in Figure S1 (Supporting Information). The initial acidic and oxidizing environment fosters the formation of Ti^{4+} via reaction (1). Owing to stable and gradual hydrolysis of melamine, the acidity is weakened followed by nucleation of TiO_2, leading to gradual growth of nanowires by reactions (2) and (3).

$$Ti + 4H^+ + 2H_2O_2 \rightarrow Ti^{4+} + 4H_2O \quad (1)$$

$$Ti^{4+} + 4H_2O \rightarrow Ti(OH)_4 + 4H^+ \quad (2)$$

$$Ti(OH)_4 \rightarrow TiO_2\downarrow + H_2O \quad (3)$$

The orientation of the nanowires can be regulated by the reaction time and initial orientation of the substrate (**Figure 1**a). After reacting for 2 h, the nanowires are tiled (sample designated as TOT for tiled TO). When the reaction time is increased to 10 h, nanowires with an average diameter of 30 nm and length of 500 nm are formed and dispersed on the substrate. The top view of the different samples can be found in Figure S2 (Supporting Information). The obliquity of nanowires as well as the number of nanofeatures (converging tips formed by nanowires) are calculated and summarized in Table S1 (Supporting Information). With regard to the samples placed horizontally and vertically in the apparatus, the nanowires grow at oblique angles of 40–50° (sample designated as TOI for inclined TO) and vertically at 80–90° (sample designated as TOV for vertical TO), respectively (red arrows in Figure 1b). The length of the nanowires can be extended to 2 µm when the reaction time is increased to 24 h (Figure S3, Supporting Information). Thereafter, TO reacts with nitrogen to form TN to improve the capacitance, while the morphology is maintained (samples designated as TNT for tiled TN, TNI for inclined TN, and TNV for vertical TN, respectively), so that both mechanical and electrical stress can be applied to adhered bacteria. The morphology of the samples is confirmed by atomic force microscopy (AFM, Figure S4, Supporting Information). While TNT shows tiled nanowires on the substrate, the nanowires on TNI grow at an angle and those on TNV are perpendicular to the substrate. The different orientations are expected to exert different shear forces on adhered bacteria to cause variable destructive effects.

The Ti—O bonding information of TOT, TOI, and TOV and transformation from T–O to T–N (TNV) are analyzed by the X-ray photoelectron spectroscopy (XPS) based on the survey spectrum (Figure S5, Supporting Information), high-resolution spectra of Ti 2p (Figures 1c,d), and semi-quantitative energy dispersive spectra (EDS, Figure S6, Supporting Information). The depth profiles of TOV show that the O:Ti ratio is roughly 2:1 indicating the formation of TiO_2 nanowires with a length of 500 nm (Figure 1e). The difference between TOV and TNV lies in the nitrogen content but there is no morphological difference. The [101] plane of TiO_2 and [200] plane of TiN are observed from the high-resolution transmission electron microscopy (TEM) images (Figure 1f). Rutile TiO_2 is the dominant phase in TO as indicated by the Raman scattering peaks at

© 2023 Wiley-VCH GmbH

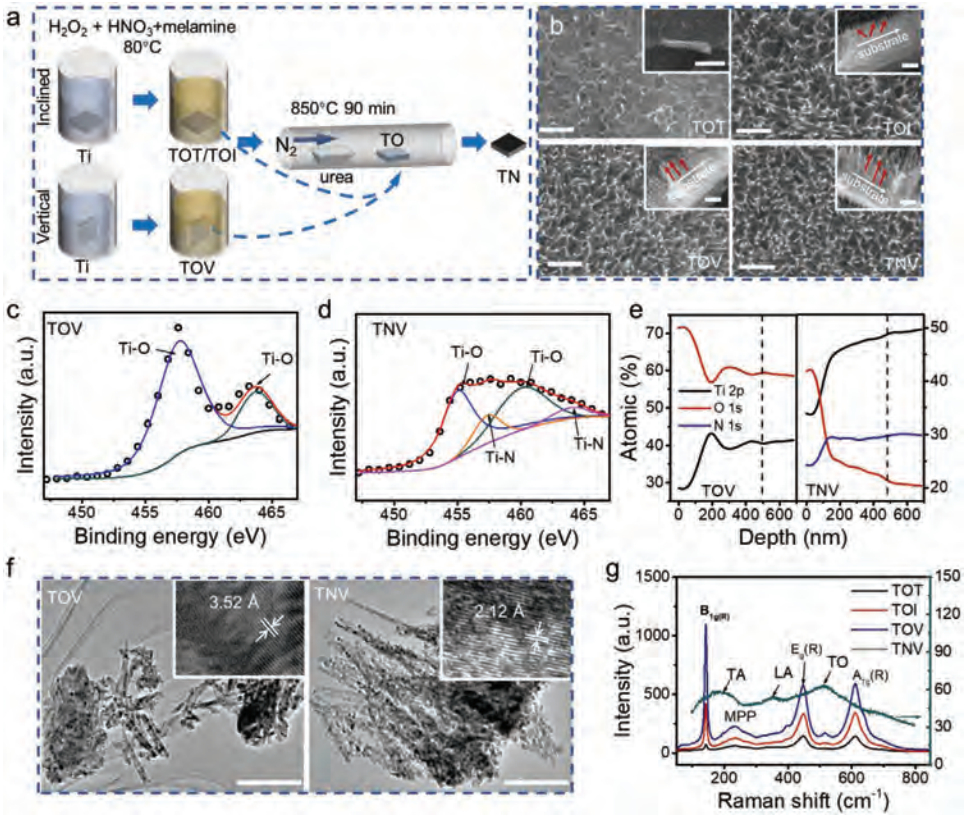

Figure 1. Sample fabrication and characterization. a) Schematic diagram illustrating the synthesis of TN nanowires with different orientations with Ti, TO, and TN denoting the titanium substrate, titanium oxide samples, and titanium nitride samples, respectively. b) Morphology of the samples by scanning electron microscopy (SEM) with the orientation of the nanowires indicated by red arrows in the insets (scale bars = 500 nm). c,d) High-resolution spectra of Ti 2p of TOV (c) and TNV (d) indicating nitrogen incorporation. e) XPS depth profiles showing the distribution of Ti, O, and N in TOV and TNV. f) High-resolution TEM images of TOV and TNV exhibiting the overall morphology and the planes are labeled in the insets (scale bars = 200 nm). g) Raman scattering spectra showing the characteristic peaks of rutile TiO_2 and TiN.

144, 394, 514, and 634 cm^{-1}. The Raman peaks of TNV at 210–230, 310–330, and 540–560 cm^{-1} correspond to the transverse acoustic, longitudinal acoustic, and transverse optical modes of TiN nanocrystals (Figure 1g) consistent with X-ray diffraction (XRD, Figure S7, Supporting Information).

The addition of melamine not only regulates the pH during the aqueous reaction, but also serves as the soft template, the symmetry of which affects the stacking and growth of TiO_2 resulting in the formation of nanowires but no other nanostructures. The horizontally placed substrates are located on the edge of the convection, whereas the vertically placed ones are at the center part of the convection where the larger diffusion rate promotes reactant etching of the substrate.[25–27] Therefore, TOV is etched more quickly and TiO_2 (anatase) precipitation generates more nanowires with a larger density to foster closer alignment and avoid significant inclination. Compared to the rutile phase, nitridation of the anatase phase is easier thus giving rise to better electrochemical properties[28] in addition to antibacterial characteristics. These results confirm the formation of TO and TN with the predesigned morphological, crystalline, and chemical properties.

As electrical interactions play an important role in the antibacterial process, the electrochemical properties of the samples are determined. The cyclic voltammetry (CV) curves acquired from TO and TN at a scanning rate of 100 mV s^{-1} are presented in **Figure 2**a and Figure S8a (Supporting Information). TOT, TOI, and TOV do not show an obvious electrochemical double-layer (EDL, Figure S8a, Supporting Information) as opposed to the typical EDL capacitive characteristics observed from TNT, TNI, and TNV. Furthermore, the CV profile of TNV shows the maximum area and largest capacitance. The galvanostatic charging–discharging (GCD) plots display a trend similar to CV with TN performing better than TO and TNV showing the longest charging and discharging time (Figure 2b; Figure S8b, Supporting Information). The maximum capacitance of 0.61 F cm^{-2} is calculated from TNV and it is slightly higher than but at a similar level as that observed previously.[17] The discharging curves of the fully charged samples are displayed in Figure 2c–e. While TO shows a flat line overlapping the *x*-axis, TN discharges a high current in the early stage (0–1000 s, Figure 2c,d) and the current decreases gradually for a duration of more than 6 h. The real-time absolute currents of the TN groups follow the order of TNT < TNI < TNV, indicating the largest capacitance of TNV, which is also verified by the capacity analysis in Figure 2f. TNV discharges 0.08 C which is several times larger than that of TNI and TNT and orders of magnitude larger than that of TO (Figure 2f). The electrochemical characteristics depend on the orientation and composition

© 2023 Wiley-VCH GmbH

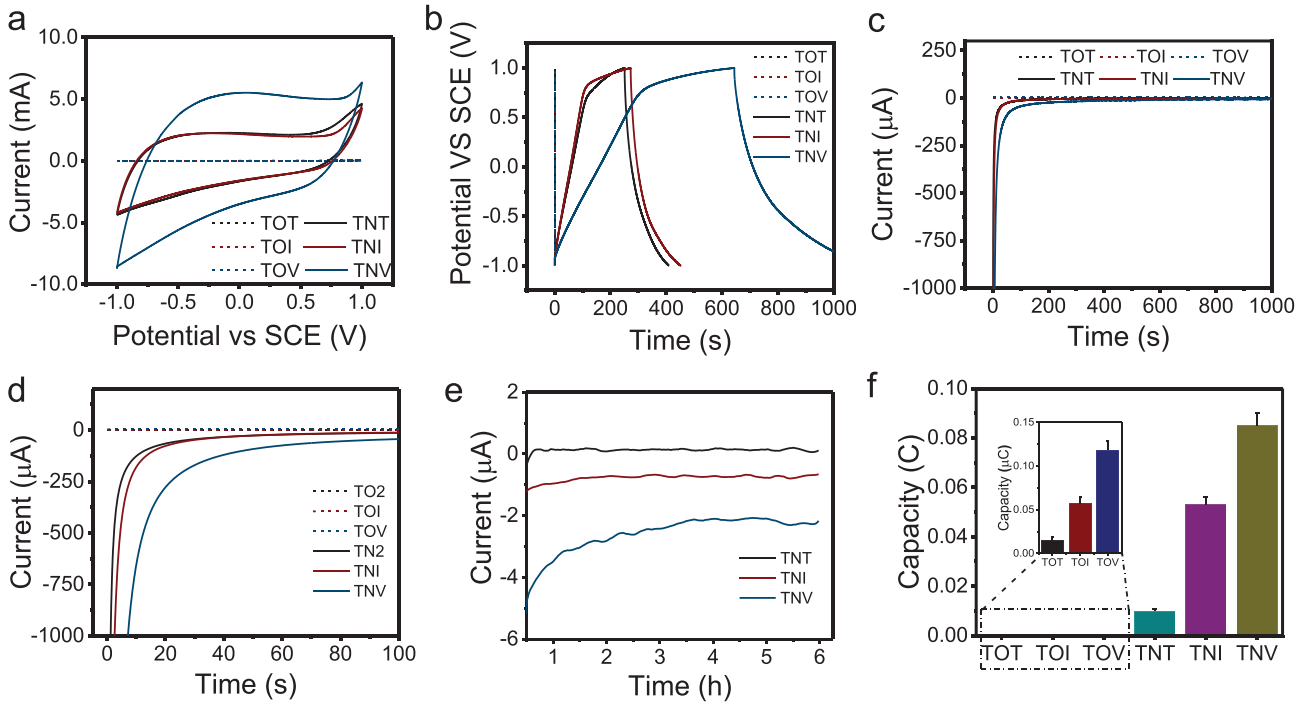

Figure 2. Electrochemical properties of TO and TN samples. a) Cyclic voltammetry (CV) curves acquired at 100 mV s^{-1} from the second cycle with the curves covering a larger area indicating a higher capacitance (Please refer to Figure S8, Supporting Information for details of TO samples). b) Galvanostatic charging–discharging curves acquired at 2.5 mA cm^{-2} from the second cycle with the longer discharging time indicating a higher capacitance (Please refer to Figure S8, Supporting Information for details of TO samples). c–e) Discharging curve obtained in the first 1000 s (c), 100 s (d), and 6 h (e) after charging TO and TN samples to 2 V. f) Total discharging capacity of the different samples after charging for 15 min as calculated from the *i–t* curve in (e). The electrochemical test is carried out in a three-electrode cell in the Lysogeny broth (LB).

of the nanowires. The smaller redox potential after N doping is more than enough to account for the substantial capacitance increase.[29] The sparsely tiled nanowires on TNT do not favor electron transfer, whereas improvement is observed from the inclined nanowires on TNI. However, compared to the randomly distributed nanowires on TNI, the vertically aligned nanowires on TNV enhance electron transfer with a larger energy storage density.[30] The charged TNV can transfer more electrons to bacteria upon contact to boost the antibacterial efficiency, which will be verified in the following sections.

3. Antibacterial Effects Under Different Conditions

The real-time bacterial viability at 1 h is evaluated by live/dead staining (**Figure 3**a). Both Gram-positive and Gram-negative bacteria can grow, proliferate, and maintain active viability on the titanium substrate (control). TNV provides a tougher environment with many bacteria showing red fluorescence, but there are still dots emitting green fluorescence. In contrast, +TNV reveals widespread red fluorescence and reduced bacteria intensity.

The samples with different nanostructures are subjected to antibacterial tests for 6 h in which both the mechanical and electrical interactions are taken into consideration. The nanowires with different orientations kill *Escherichia coli* differently. After 6 h, 40% of the bacteria on TOT are killed (0.22 log reduction), whereas the inclined nanowires on TOI can eliminate 55% of the bacteria (0.36 log reduction, Figure 3b). In comparison, the vertical nanowires on TOV kill 75% of the bacteria (0.62 log reduction), which is the same as TNV despite the different compositions (Figure 3c). Besides, the longer nanowires do not contribute much to the antibacterial efficiency as there is no significant difference between the antibacterial rates of TNV24 and TNV10 groups (Figure S9, Supporting Information). As aforementioned, an antibacterial efficacy of 75% is unsatisfactory because a substantial number of bacteria can regrow after a few hours. In this respect, the charged TNV (+TNV) exhibits an antibacterial ability of 99.9% against *E. coli* (≈3 log reduction, Figure 3c). The insignificant antibacterial effects of electrically charged TOV (+TOV) indicate that capacitance plays a significant role in the antibacterial process. +TOV with little capacitance cannot transfer enough charge to the adhered bacteria thus bringing little improvement to the antibacterial ability (Figures 2 and 3c). A similar tendency is observed from Gram-positive bacteria *Staphylococcus aureus*. TOV and TNV with vertical nanowires fare the best (≈60%, 0.4 log reduction) among the uncharged samples, while +TNV after charging shows an antibacterial rate of more than 99% (≈2 log reduction, Figures 3d,e). The antibacterial efficiency is further verified by two other strains of bacteria (*Pseudomonas aeruginosa* and *Staphylococcus epidermidis*, Figures S10 and S11, Supporting Information). These results indicate that while the double-enhanced antibacterial ability can be achieved by adjusting the orientation of nanowires,

© 2023 Wiley-VCH GmbH

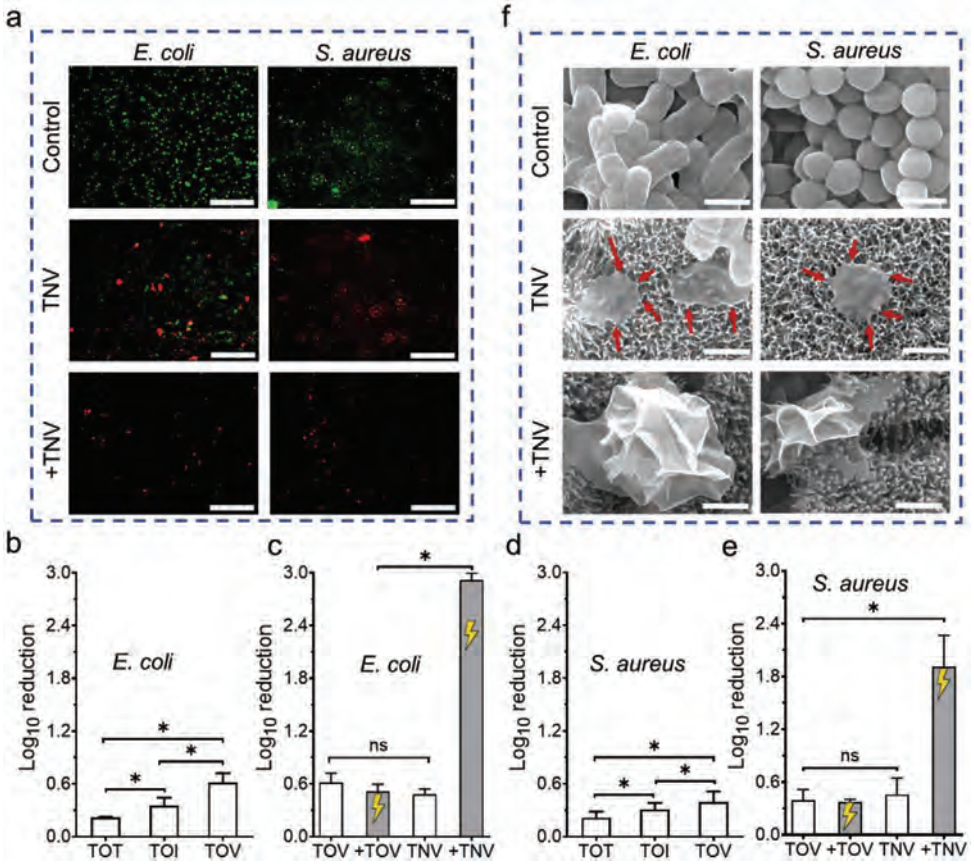

Figure 3. Antibacterial properties of the different samples under different conditions. a) Real-time viability of *E. coli* and *S. aureus* on the different (charged) samples obtained by live/dead staining (scale bars = 50 µm). b) Antibacterial effects comparison of mechanical forces exerted by nanowires with different orientations against *E. coli*. c) Antibacterial effects comparison of electro–mechanical forces against *E. coli*. d) Antibacterial effects comparison of mechanical forces exerted by nanowires with different orientations against *S. aureus*. e) Antibacterial effects comparison of electro–mechanical forces against *S. aureus*. f) Bacterial morphology after cultivation on the different (charged) samples for 24 h (scale bars = 1 µm).

a strikingly 5 times increase can be further accomplished by taking advantage of the capacitance. As the capacitance of TNV has a similar level as that of carbon-doped titanium dioxide nanotubes,[17] the enhanced antibacterial ability is deemed to be closely associated with both the mechanical and electrical interactions at the interface.

How the charging modes influence the antibacterial ability is explored. Positive charging fares much better than negative charging (Figure S12, Supporting Information) because the positive charge yields a larger potential difference to elevate electron transfer at the interface. A larger charging voltage increases the charges and more than 3 log reduction is achieved by 4 V (Figure S13, Supporting Information). A charging voltage of 2 V is chosen for the subsequent work.

As aforementioned, bacteria are killed by the combination of mechanical and electrical interaction and therefore, an intuitive phenomenon should be the bacterial morphological change. As shown in Figure 3f, the titanium substrate as the control is covered by a large density of *E. coli*, which maintains the typical rod shape with a length of 2 µm and diameter of 0.5 µm. The tiled nanowires on TNT hinder the proliferation of bacteria and some of them are slightly shriveled (Figure S14, Supporting Information). The inclined nanowires on TNI cause the bacterial membrane to collapse (Figure S14, Supporting Information) and the vertical nanowires on TNV even flatten the whole cell (red arrows in Figure 3f). Electrical charges further cause severe distortion so that the original rod-like morphology can no longer be recognized. *S. aureus* exhibits a similar morphological change trend, that is, a smooth spherical shape on titanium, lumpier and craggier membrane on TNT and TNV, and obvious disruption on +TNV. The morphological change illustrates that progressive stress is exerted on the bacteria in the order of TNT < TNI < TNV < +TNV. The morphological disruption by +TNV is universal as shown by the images at lower magnification (Figure S14, Supporting Information). Besides, the bacteria wreckages sparsely locate on the surface of +TNV indicating the efficient antibacterial ability. For the bacteria on +TNV, the potential difference between the positively charged TNV and negatively charged bacteria membrane enhances the electrostatic attraction and therefore, the membrane adheres more tightly to the surface with vertical nanowires and consequently, larger surface tension is exerted onto the bacteria.[3,31,32] However, we cannot conclude unequivocally that the nanowires are more suitable for bacteria adhesion because fewer bacteria are found on +TNV and charging fixes the bacteria so that they can no longer detach or move for metabolism.[33] Besides, the

© 2023 Wiley-VCH GmbH

potential difference may also disrupt the equilibrium of electrons in the respiration chain. These biomechanical and electrical interactions work in concert to enhance the antibacterial properties.

4. Biophysical Antibacterial Mechanism

4.1. Visual Images Providing Qualitative Information about the Topography and Adhesion Force

The biophysical changes during the bacteria-materials interactions are studied to fathom the bacteria-killing process. The surface topography and potential maps of the samples are acquired from a 5 μm × 5 μm area by AFM using the tapping mode as shown in **Figure 4**a and Figure S15 (Supporting Information). The 3D surface topographical images impart information about the bacteria's location (2D image) as well as height from the surface (brightness, Figure S15, Supporting Information). The distribution of bacteria is similar to that disclosed by SEM. The bacteria density on the control and TNT is so large that the substrate can hardly be recognized. In contrast, fewer bacteria adhere to the surface of TNI, TNV, and +TNV and morphological disruptions are detected (black arrows in Figure S15, Supporting Information). The bacteria on +TNV are deformed most severely indicative of the harshest environment after charging. The brightness in the potential maps reflects the irregular bacterial shape (Figure 4a). Bright edges are detected from TNI and TNV and the brightest points emerge from +TNV, indicating the largest shape change on the membrane caused by the electro–mechanical interaction (white arrows in Figure 4a).

4.2. Analysis of the Adhesion Force and Membrane Stiffness

The antibacterial trend from TNT to +TNV is investigated quantitatively by AFM. The force–distance curves show both the adherence force[34] and bacterial stiffness.[35,36] The nonlinear portion in the retraction curve is used to determine the adhesion force between the bacteria and substrate (Figure 4b) and the retracted curve in Figure 4c conveys semi-quantitative information. The adherence force between the titanium plate and bacteria is the weakest but increases on the nanowires or charged surface. The quantitative results in Figure 4d show that the adherence forces on the control and TNT are about the same as 20 nN and it increases to 23 nN for TNI despite the statistical insignificance (TNT vs TNI). It continues to increase by more than 50% to 30 nN and 35 nN on TNV and +TNV with significant differences ($p < 0.05$), respectively. The adhesion force of +TNV is larger than the threshold of bacteria and is in the lethal regime (>10 nN) reported previously.[37,38] Besides, the stiffness of the bacteria membrane is elevated in the order of control < TNT < TNI < TNV < +TNV with significant differences in all the experimental groups compared with the control group (Figure 4e). As the tip moves within tens of nanometers which are smaller than the size of bacteria, it touches the bacteria membrane but not the substrate. Hence, the different topographies of the substrate are supposed to make little difference. The stiffness is closely related to the extension force imposed on the outer membrane.[39] For a small tension, self-adjustment of the flexible membrane maintains the area but when the tension increases so much that membrane undulation is no longer possible. The stress turns into stretching forces from various directions around the bacteria. The entire membrane is gradually flattened and the stiffness increases exponentially.[40] Owing to the strong tension on TNV and even stronger tension on +TNV, the stiffened membrane becomes crisp and fragile.

4.3. Simulation of the Interactions and Influence on Membranes

The bacteria-surface interactions are analyzed by molecular dynamic simulation and demonstrated in the videos. Without applying an electric field to the bilayer in the nanowire system (Figure 4f; Video S1, Supporting Information), it takes 50 ns for the nanowire to get in close contact with the bilayer. The electric field significantly increases the approaching velocity. At 20 mV, the nanowire interacts with the bilayer for 30 ns but still does not translate through it (Figure 4f; Video S2, Supporting Information). However, when the electric field is increased to 200 mV, the same nanowire takes only 1.1 ns to translate and break the bilayer (Figure 4f; Video S3, Supporting Information). A small morphological change is observed from the bilayer at 20 mV, while the bilayer suffers serious distortion at 200 mV.

Membrane distortion is quantitatively analyzed on the nanosecond scale by calculating the Gaussian curvature in the system (Figure 4g,h). The Gaussian curvature increases from 1.91×10^{-6} (Upper = 3.73×10^{-6}, Lower = 9.39×10^{-8}) for the bilayer membrane in non-voltage simulation to 7.15×10^{-3} (Upper = 4.7×10^{-3}, Lower = 9.6×10^{-3}) for 20 mV, confirming the narrowed and bumped interface as a result of electrostatic interactions. The area compressibility modulus K_A of the treated bilayer which is correlated positively with the stiffness and Young's modulus is considered (Figure 4i). K_A increases from 190 ± 25.1 mN m^{-1} for the non-voltage trajectory to 256 ± 32.1 mN m^{-1} for 20 mV. Both the enhanced curvature and K_A contribute to a stiffer membrane, making it easier to be penetrated and destroyed.[41] All in all, the simulation results are consistent with the experimental data, illustrating that +TNV has stronger adhesion force to narrow the interface and the stiffer membrane renders it more susceptible to disruption.

The adhesion strength at the interface is crucial to bacteria destruction and a larger adhesion force is expected to lead to a higher probability of rupturing for the same nanostructure morphology.[42,43] When bacteria are in contact with the nanowires, they will try to settle on the rugged and stiff surface by increasing the contact area and anchor on multiple points (red arrows in Figure 3f). However, this stretching process may exert surface tension surpassing the threshold of the bacteria membrane, in which case cell rupture can take place at any time. The electrical attraction between the charged TNV and bacteria makes the bumped surface tougher and as a result, serious membrane collapse arising from the maximum electro–mechanical stress is observed from +TNV. Hence, the electro–mechanical interactions on +TNV accentuate the mechanical disruption of the bacteria.

© 2023 Wiley-VCH GmbH

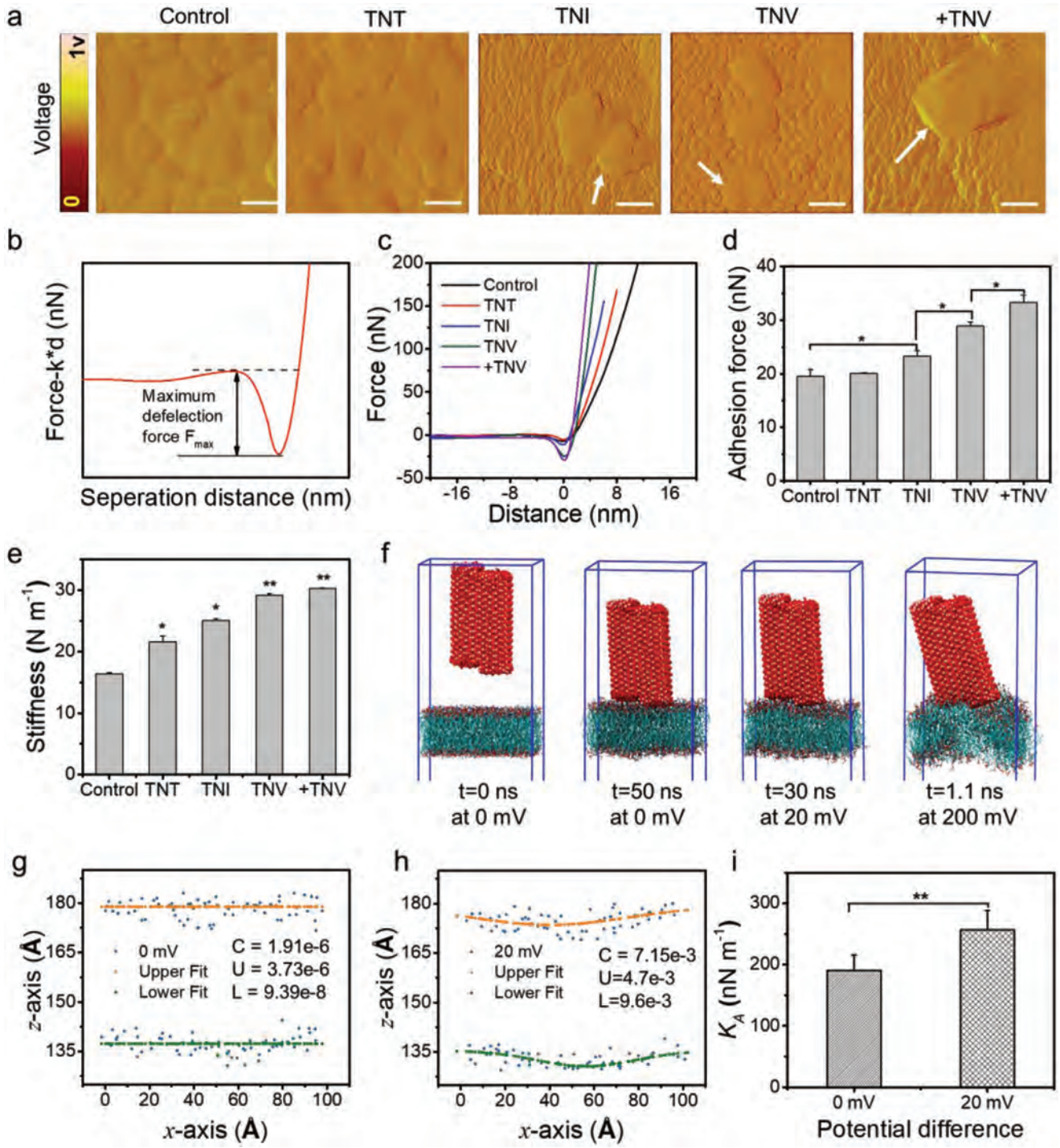

Figure 4. Biophysical antibacterial mechanism. a) Potential maps of bacteria cultivated on different samples in an area of 5 μm × 5 μm illustrating cohesion at the interface (scale bars = 1 μm). b) Schematic diagram showing how the retracted line reflects the adherence force; c) Retracted force–distance curve of the AFM tip from the bacteria on different samples. d) Adhesion force between the bacteria and sample surface calculated from the non-linear part of the retracted curves in (c). e) Membrane stiffness calculated from the linear part of the curves in (c). f) Simulated interface between the sample surface and bilayer at different time under different conditions. g,h) Gaussian curvature fitting of the bilayer in non-voltage (g) and voltage (h) trajectories. i) Area compressibility modulus K_A of the bilayer after interacting with the surfaces with/without charging.

5. Biochemical Antibacterial Mechanism

Apart from the mechanical force exerted on bacteria, the electrically charged surface is expected to interact with the negatively charged outer membrane of bacteria causing electron disbalance. To explore the potential difference at the interface and the ensuing physical changes of the bacteria, the membrane potential and intracellular electron density are determined.

© 2023 Wiley-VCH GmbH

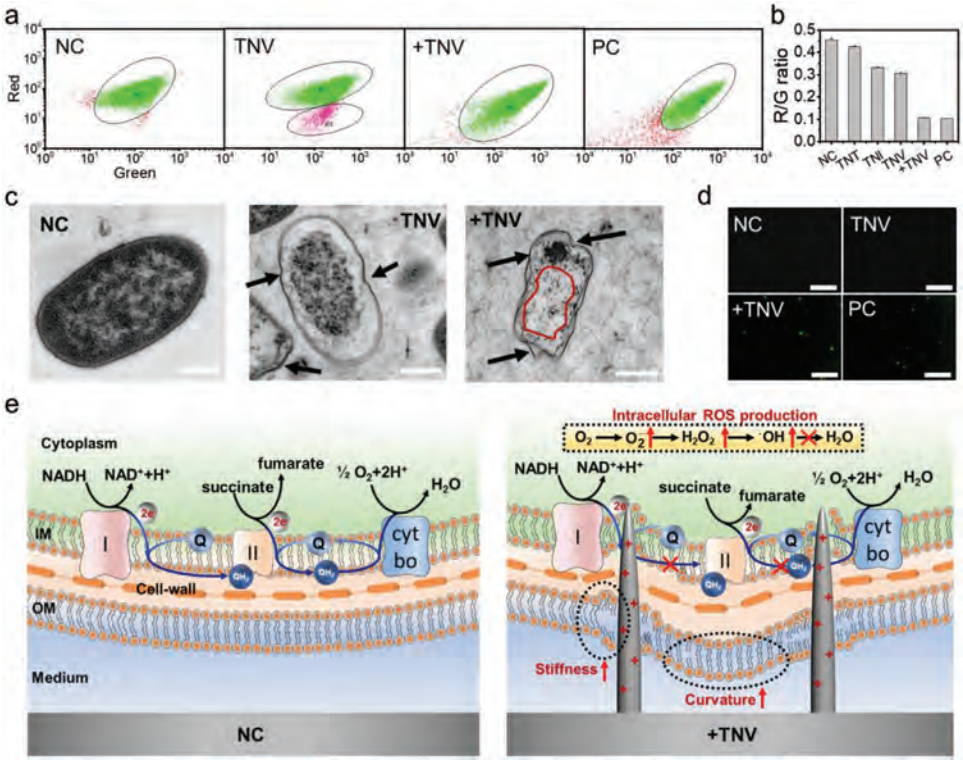

Figure 5. Biochemical antibacterial mechanism. a) Dots emitting red/green fluorescence after staining the membrane by the potential kit and detected by flow cytometry with gates to exclude the debris. The bacteria in TNV are distributed in two regions due to different states of the membrane potentials. b) Quantitative comparison of the membrane potentials characterized as R/G ratios. c) TEM images of the bacteria on the different samples (scale bars = 500 nm). d) Fluorescent staining images of intracellular ROS of the bacteria on the different samples (scale bars = 50 μm). e) Schematic diagrams showing how bacteria are affected on the different surfaces. NC shows the normal state of bacterial membrane with intact lipid bilayers and respiration chain. +TNV shows that the vertical nanowires exert intense mechanical tension to the lipid bilayer that the lipid molecules are no longer orderly arranged with increased stiffness and curvature on the mesoscopic scale. Besides, electron transfer of the respiration chain is disrupted by the charged surface that accumulation of ROS takes place. The electro–mechanical interaction is most lethal to bacteria. NC = negative control and PC = positive control.

5.1. Membrane Potential Reduction

The membrane potential which is an indicator of the polarization state of bacteria can be expressed by the red/green (R/G) ratio after staining by $DiOC_2(3)$. Normally polarized bacteria are supported by a negative membrane potential with a relatively large R/G ratio. As shown in **Figure 5**a and Figure S16, Supporting Information, the membrane potential on the control and TNT is about the same, but on TNI and TNV, the bacteria are distributed in two regions (R2 and R3). The membrane potential of R2 is similar to that of the control group, but that of R3 decreases significantly, revealing that TNI and TNV disrupt the bacteria upon direct contact. However, other bacteria that do not make direct contact (R2) are not affected. When TNV is charged before bacteria culturing, the whole quorum of bacteria are marked with a significantly reduced R/G ratio similar to the positive control group (PC), indicating that +TNV influences bacteria in a wider range than TNV. The corresponding quantitative results are presented in Figure 5b. The slightly reduced R/G ratio can be explained by the mechanical damage to the adhered bacteria at the very top of TNI and TNV, whereas more than 3 times reduction of R/G is observed from +TNV on account of the enhanced mechanical and electrical interferences on the bacteria. The membrane potential difference among the groups suggests that the nanomechanical interactions at the interface slightly neutralizes the resting potential by increasing the membrane permeability, while the addition of positive charges decreases the permeability and triggers instantaneous electron transfer through the membrane, giving rise to multiplied reduction of the R/G ratio, which is consistent with the results reported previously.[17]

5.2. Intracellular Electron Distribution

The biochemical change rendered by the electro-chemical interactions was further examined by performing TEM on the sliced bacteria (Figure 5c; Figure S17, Supporting Information). Bacteria suffer from increasing membrane disruption in the order of TNT < TNI < TNV < +TNV (black arrows). Besides, electrons are distributed uniformly on the other samples, while +TNV shows obvious electron-light regions corresponding to electrical disbalance in the membrane potential test (area circled in red in Figure 5c). The results verify the hypothesis that while TNI or TNV causes only limited mechanical damage to the bacteria, addition of electrical charges accentuates the mechanical

© 2023 Wiley-VCH GmbH

interaction and also triggers electron flow in a specific direction. The electric field between the positive charges on the +TNV surface and negative outer membrane stimulates electron flow from the bacteria to the outside as indicated by the electron light regions. As a result, +TNV poses the harshest microenvironment for bacteria to devastate the membrane potential, which is fundamental to the proton motive force in bacteria to regulate cell division and therefore determines the living state of bacteria.[44]

5.3. Intracellular Oxidative Stress by Electron Interference

Dissipation of the membrane potential influences the availability to utilize oxygen as the electron acceptor and disorganizes the intracellular oxidative level (Figure 5d; Figure S18, Supporting Information). While TNT, TNI, and TNV are similar to the negative control showing no intracellular ROS spot, +TNV exhibits similar results as the positive group showing significant green spots. ROS staining indicates that the nanowires with different orientations only disturb the integrity of the membrane, whereas electron transfer is an important factor influencing the oxidation level. As electron suppliers, the components inside the bacteria are oxidized when electrons are depleted by the positively charged surface. The internal ROS level is raised by a series of biochemical reactions[45] which consume a lot of energy and starve the bacteria to death as a second attack besides mechanical damage. The insignificant change in the quantity of extracellular ROS indicates the nature of contact-killing and no chemical reactions are expected to take place between materials and medium (Figure S19, Supporting Information). The schematic diagram (Figure 5e; Figure S20, Supporting Information) shows how the bacteria are affected by different surfaces based on the above results and the basic theory raised in previous work.[46–49]

6. In Vitro Cytocompatibility

+TNV fares the best in the antibacterial assessment and preliminary in vitro cell experiments and there is an indication that none of the TN samples adversely affect adherence and proliferation of osteoblasts and even foster the growth of osteoblasts as indicated by MTT for 7 days (Figure S21a, Supporting Information). The cytoskeleton of the osteoblasts after culturing for 24 h is observed after fluorescent staining (Figure S21b, Supporting Information). The osteoblasts on the four TN samples adhere and proliferate well with the spreading filopodia showing a larger area than the control. The magnified SEM image shows consistent results (Figure S21c, Supporting Information). Comparing the electrically charged and uncharged groups, no significant difference can be found illustrating that it is the nanostructure that enhances adhesion and proliferation of osteoblasts.[50,51]

6.1. In Vivo Evaluation of Antiinfection and Antiinflammation

S. aureus which is most frequently found in implant-related infection was chosen for the animal model to investigate implant- and tissue-related bacteria for 5 and 10 days.[52] Although more than 75% of the bacteria on the implants and tissues in all the samples can be inactivated during the first 5 days (log reduction > 0.6), bacteria that escape initial death proliferate subsequently on TOV, +TOV, and TNV. On the other hand, the antibacterial rate of +TNV is maintained to be 99% (log reduction > 2), illustrating that the combination of nanomechanical force and electron transfer synergistically inhibits bacteria proliferation (**Figure 6**a,b). The excellent antibacterial efficiency of +TNV leads to healthy recovery without significant fibrous layers or inflammation. In contrast, a large number of bacteria survive on TNV. The fibrous layer is as thick as that in the positive control (Figure 6c, the area circled in red). Consequently, infection triggers the immunological system resulting in the aggregation of lymphocytes (black arrows in Figure 6c). The continuous antibacterial ability is believed to be attributed to both the nanostructure on the surface and the sustaining discharging ability of the charged capacitive samples (Figure 2). The in vivo results corroborate the in vitro analysis and the synergistic effects rendered by the mechanical and electrical interactions are preserved in vivo. As early infection usually takes place during the first week after implantation,[52] the in vivo results reveal the high clinical potential of this dual antibacterial strategy.

7. Discussion

Surgery is usually associated with the risk of microbial contamination, leading to amputation and mortality in serious cases. Hence, much effort has been made to prevent implant-related infections by designing antibacterial materials.[53] As infections are usually initiated from bacterial adherence on the implant surface,[54] both leaching surfaces that can release antibiotics and non-leaching surfaces have been developed to prevent bacterial adherence. However, leaching surfaces require replenishment of antibacterial agents with possible systemic side effects such as drug resistance.[55] Therefore, non-leaching surfaces which kill bacteria based on physical interactions causing little exhaustion or disturbance in the distal tissue are becoming more prevalent.[56–58] In this work, TN nanowires with different orientations are prepared by controlling the reaction time and the placement locations of the substrates. In principle, the formation of titania nanowires stems from heterogeneous nucleation and precipitation from the ambient solution rather than sedimentation of the products under gravity. Besides, thermal convection in the solution and thermal diffusion of the solute account for the different alignments of the nanowires. Hence, nanowires can grow on arbitrary surfaces provided that the reaction and fabrication parameters are optimized to maintain the desirable convection state on the different surfaces. The methodology described herein imparts valuable information about the fabrication of oriented nanostructures by exploiting convection in the thermal chemical reaction.

A quantifiable relationship between antibacterial efficiency and electro–mechanical force is derived in this work. Without electrical charging, compared to the tiled (TNT) and inclined (TNI) nanowires, the vertical ones (TNV) kill the largest percentage of bacteria (Figure 3) by stretching the

© 2023 Wiley-VCH GmbH

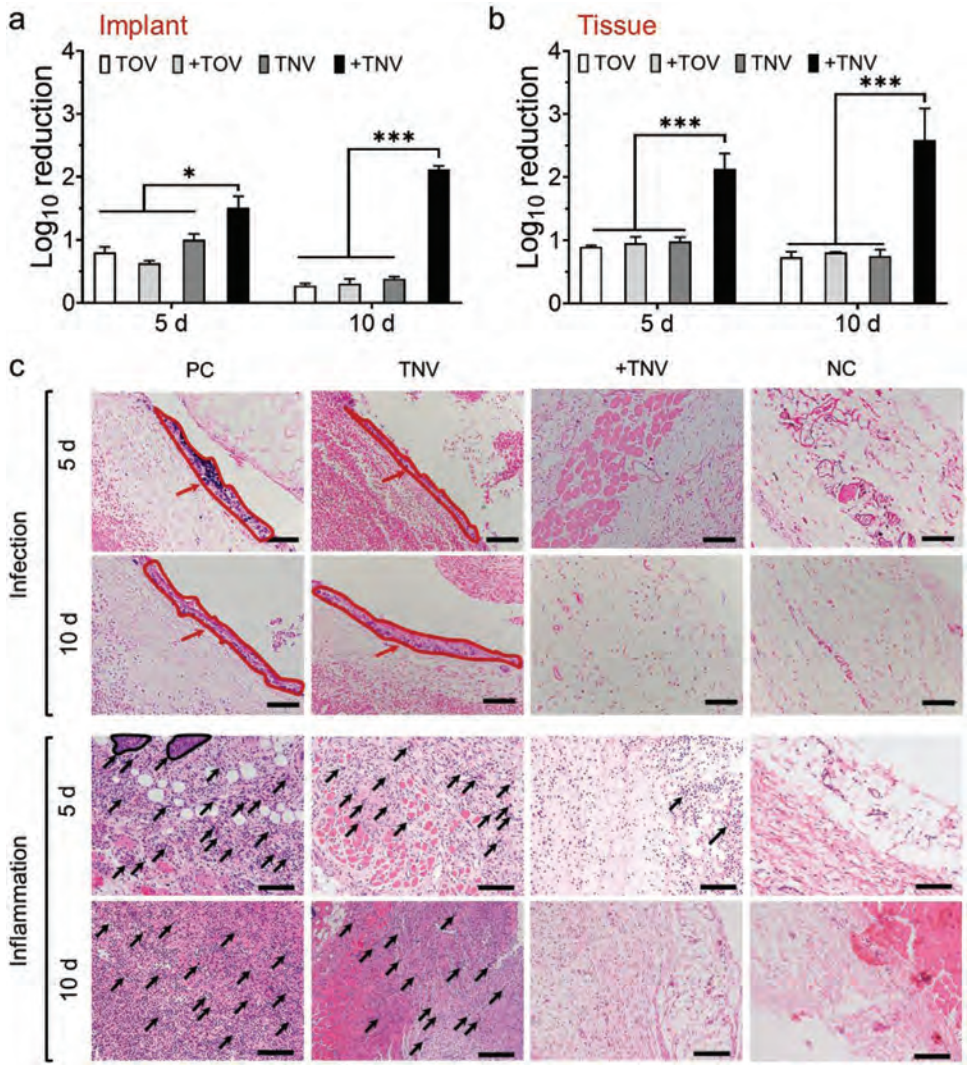

Figure 6. In vivo experiments evaluating antiinfection and antiinflammation. a,b) Antibacterial results from surgical implant (a) and surrounding tissues (b) 5 and 10 days after bacteria challenge. c) Infection and inflammation state of the surrounding tissues after Gram and H&E staining, respectively (scale bars = 100 µm). The infected areas are circled in red and marked with red arrows and the inflammation parts are marked with black arrows.

bacterial membrane. It has been demonstrated that nanostructures can kill bacteria by piercing the bacteria membrane, a phenomenon similar to that on natural structures such as cicada wings.[10,14,22] Nevertheless, quantitative analysis of the mechanical interactions and detailed information on how nanostructures can be tuned to control the antibacterial performance are lacking. In this work, the enhanced antibacterial efficiency can be explained quantitatively by the 1.5 times larger adhesion force arising from the elevated van der Waals force.[22] Shear force is generated when adhered bacteria try to move away from the surface and there is a chance for membrane damage, which destroys the membrane integrity and causes death.[59] Although vertical nanowires kill bacteria with the highest efficacy, 20% of the bacteria are still alive and can proliferate subsequently resulting in the declining antibacterial rates from 5 to 10 days observed from the animal experiments on TOV and TNV (Figure 6). This is consistent with previous works in which biofilm growth is not eradicated but is only slowed by the mechanical force exerted by cicada wings or the bio-inspired nanostructure.[60] Besides, the platform based on capacitance in our previous work can only kill 80% of the *E. coli* by one-time charging. Hence, neither passive mechanical disruption nor charging alone is enough to mitigate bacterial infection. As described in this paper, in order to boost the antibacterial properties, mechanical interactions are supplemented with electrical ones and consequently, 2–3 log reduction is accomplished both in vitro and in vivo. The mechanism works on both Gram-positive and Gram-negative bacteria because mechanical and electrical forces in different degrees form in both cases. The enhanced antibacterial efficiency can prevent recurring infection, as verified by the bacteria number and the infection state after 5 and 10 days. Apart from developing new antibacterial materials, here we take into consideration both the clean antibacterial strategy and efficient antibacterial efficacy, to which much attention should be paid in developing biomedical implants with clinical viability.

© 2023 Wiley-VCH GmbH

Both experimental and simulative models are established here to explain how gradient electrical and mechanical forces work complementarily to cause harm to bacteria.[39] TNV with considerable capacitance is verified electrochemically[61] and the electrostatic force is demonstrated to be sufficient to cause membrane damage in concert with mechanical stress. The rugged topography formed by the nanowires exerts enhanced stretching forces on the membrane and the elevated stiffness increases the damage to the bacteria (Figures 3 and 4). The experimental data are supported by theoretical simulation that when the potential difference is increased from 0 to 200 mV, closer contact is created in 1.1 ns and the transformed bilayer with an increased Gaussian curvature and K_A indicates a stiffened membrane. The sufficient mechanical contact reinforces electron transfer as validated by the membrane potential and light regions inside the bacteria observed from +TNV (Figure 5). The electrical disbalance contributes to oxidation-reduction turbulence in the intracellular part exhibited as elevated ROS on +TNV but not the other groups. Hence, the bacteria in the comparatively large vicinity experience membrane and intracellular disruption. The experimental and theoretical investigations provide quantitative information on how electro–mechanical stress can be regulated to boost the antibacterial ability and mitigate bacterial infection.

In the practical application, mechanical and electrical forces can be tuned orthogonally to meet the requirement for specific antibacterial efficiency. For instance, morphological adjustment is enough for 80% bacterial reduction and more attention should be paid to the capacitance optimization or charging voltage if the bacterial contamination is expected to be serious and more than 99.9% antibacterial reduction is required. Hence, the quantifiable relationship between biophysical forces and antibacterial efficiency and the revealed antibacterial mechanism demonstrated in this work provide a principle for antibacterial implant design, which will be of interest to both biomaterologists and clinicians. As this platform has potential applications besides biomedical implants, more in-depth studies will be performed to validate the individual requirements and efficacy for applications in wearable devices or environmental engineering, etc.

8. Conclusion

Capacitive nanowires with different orientations are produced to enhance the antibacterial properties. The quantitative relationship between electro–mechanical interactions and antibacterial efficacy is established. Compared to the tiled and inclined nanowires (TNT and TNI) showing log reduction of less than 0.4, nanowires with the vertical orientation (TNV) kill 0.6 log of the bacteria by stretching the membrane. The antibacterial efficiency can be further enhanced by five times to ≈3 log reduction by charging the capacitive TNV (+TNV) and the latter process is demonstrated to rescue rats from a bacterial infection in vivo. The systematic biophysical, electrochemical, and biochemical analyses provide clues that the electrical interactions not only supplement mechanical damage by accentuating the electrostatic attraction between the bacteria and implant surface, but also facilitate electron flow from bacteria to the surface to enhance intracellular ROS production. As result, bacteria die from the dual effects of membrane damage and intracellular oxidative stress. The biophysical and biochemical analyses provide insights into the development of non-leaching antibacterial implant materials with clinical significance.

Supporting Information

Supporting Information is available from the Wiley Online Library or from the author.

Acknowledgements

The authors acknowledge financial support from Hong Kong PDFS – RGC Postdoctoral Fellowship Scheme (PDFS2122-1S08 and CityU 9061014), Hong Kong HMRF (Health and Medical Research Fund) (2120972 and CityU 9211320), NSFC (21925505), Shanghai international scientific collaboration fund (21520710100), Innovation Program of Shanghai Municipal Education Commission (2023ZKZD28). J.D. is the recipient of a National Science Fund for Distinguished Young Scholars and G.W. is the recipient of the National Natural Science Fund for Excellent Young Scientists (Oversea). The authors acknowledge Dr. Peng GAO and Dr. Richard Yi Tsun KAO from The University of Hong Kong for providing the bacterial strains.

Conflict of Interest

The authors declare no conflict of interest.

Data Availability Statement

The data that support the findings of this study are available from the corresponding author upon reasonable request.

Keywords

antibacterial surfaces, bioelectrical, biomechanical, electro–mechanical forces, molecular dynamics

Received: December 31, 2022
Revised: January 29, 2023
Published online: March 22, 2023

[1] Q. Zheng, X. Liu, Y. Zheng, K. W. Yeung, Z. Cui, Y. Liang, Z. Li, S. Zhu, X. Wang, S. Wu, *Chem. Soc. Rev.* **2021**, *50*, 5086.
[2] H. Murata, R. R. Koepsel, K. Matyjaszewski, A. J. Russell, *Biomaterials* **2007**, *28*, 4870.
[3] J. Hasan, R. J. Crawford, E. P. Ivanova, *Trends Biotechnol.* **2013**, *31*, 295.
[4] D. P. Linklater, V. A. Baulin, X. L.e Guével, J. B. Fleury, E. Hanssen, T. H. P. Nguyen, S. Juodkazis, G. Bryant, R. J. Crawford, P. Stoodley, *Adv. Mater.* **2020**, *32*, 2005679.
[5] B. Mehrjou, S. Mo, D. Dehghan-Baniani, G. Wang, A. M. Qasim, P. K. Chu, *ACS Appl. Mater. Interfaces* **2019**, *11*, 31605.
[6] E.-J. Kim, M. Choi, H. Y. Park, J. Y. Hwang, H.-E. Kim, S. W. Hong, J. Lee, K. Yong, W. Kim, *Sci. Rep.* **2019**, *9*, 13697.

 © 2023 Wiley-VCH GmbH

[7] T. Ma, X. Zhai, Y. Huang, M. Zhang, X. Zhao, Y. Du, C. Yan, *Adv. Healthcare Mater.* **2021**, *10*, 2100033.
[8] X. Lu, X. Feng, J. R. Werber, C. Chu, I. Zucker, J. H. Kim, C. O. Osuji, M. Elimelech, *Proc. Natl. Acad. Sci. USA* **2017**, *114*, E9793.
[9] G. Wang, W. Jiang, S. Mo, L. Xie, Q. Liao, L. Hu, Q. Ruan, K. Tang, B. Mehrjou, M. Liu, L. Tong, H. Wang, J. Zhuang, G. Wu, P. K. Chu, *Adv. Sci.* **2020**, *7*, 1902089.
[10] E. P. Ivanova, J. Hasan, H. K. Webb, V. K. Truong, G. S. Watson, J. A. Watson, V. A. Baulin, S. Pogodin, J. Y. Wang, M. J. Tobin, C. Lobbe, R. J. Crawford, *Small* **2012**, *8*, 2489.
[11] E. P. Ivanova, J. Hasan, H. K. Webb, G. Gervinskas, S. Juodkazis, V. K. Truong, A. H. Wu, R. N. Lamb, V. A. Baulin, G. S. Watson, *Nat. Commun.* **2013**, *4*, 2838.
[12] S. Pandit, Z. Cao, V. R. S. S. Mokkapati, E. Celauro, A. Yurgens, M. Lovmar, F. Westerlund, J. Sun, I. Mijakovic, *Adv. Mater. Interfaces* **2018**, *5*, 1701331.
[13] S. Kim, U. T. Jung, S.-K. Kim, J.-H. Lee, H. S. Choi, C.-S. Kim, M. Y. Jeong, *ACS Appl. Mater. Interfaces* **2015**, *7*, 326.
[14] J. Jenkins, J. Mantell, C. Neal, A. Gholinia, P. Verkade, A. H. Nobbs, B. Su, *Nat. Commun.* **2020**, *11*, 1626.
[15] G. Wang, W. Jin, A. M. Qasim, A. Gao, X. Peng, W. Li, H. Feng, P. K. Chu, *Biomaterials* **2017**, *124*, 25.
[16] R. A. Marcus, *Rev. Mod. Phys.* **1993**, *65*, 599.
[17] G. Wang, H. Feng, L. Hu, W. Jin, Q. Hao, A. Gao, X. Peng, W. Li, K. Y. Wong, H. Wang, Z. Li, P. K. Chu, *Nat. Commun.* **2018**, *9*, 2055.
[18] S. Panda, T. K. Rout, A. D. Prusty, P. M. Ajayan, S. Nayak, *Adv. Mater.* **2018**, *30*, 1702149.
[19] Y. Li, X. Xu, X. Liu, B. Li, Y. Han, Y. Zheng, D. f. Chen, K. W. K. Yeung, Z. Cui, Z. Li, *Adv. Sci.* **2020**, *7*, 2000023.
[20] W. E. Thomas, E. Trintchina, M. Forero, V. Vogel, E. V. Sokurenko, *Cell* **2002**, *109*, 913.
[21] J. Xu, K. Qu, J. Zhao, X. Jian, Z. Gao, J. Xu, Y.-Y. Song, *Anal. Chem.* **2019**, *92*, 2323.
[22] C. D. Bandara, S. Singh, I. O. Afara, A. Wolff, T. Tesfamichael, K. Ostrikov, A. Oloyede, *ACS Appl. Mater. Interfaces* **2017**, *9*, 6746.
[23] G. Hazell, P. W. May, P. Taylor, A. H. Nobbs, C. Welch, B. Su, *Biomater. Sci.* **2018**, *6*, 1424.
[24] G. Reguera, K. D. McCarthy, T. Mehta, J. S. Nicoll, M. T. Tuominen, D. R. Lovley, *Nature* **2005**, *435*, 1098.
[25] W. Guo, Y. Li, Y. Tang, S. Chen, Z. Liu, L. Wang, Y. Zhao, F. Gao, *Electrochim. Acta* **2017**, *229*, 197.
[26] Z.-Y. Ma, Z.-L. Yu, Z.-L. Xu, L.-F. Bu, H.-R. Liu, Y.-B. Zhu, B. Qin, T. Ma, H.-J. Zhan, L. Xu, *Matter* **2020**, *2*, 1270.
[27] E. A. Rietman, D. E. Friesen, P. Hahnfeldt, R. Gatenby, L. Hlatky, J. A. Tuszynski, *Theor Biol Med Model* **2013**, *10*, 39.
[28] T. Luttrell, S. Halpegamage, J. Tao, A. Kramer, E. Sutter, M. Batzill, *Sci. Rep.* **2014**, *4*, 4043.
[29] T. Lin, I.-W. Chen, F. Liu, C. Yang, H. Bi, F. Xu, F. Huang, *Science* **2015**, *350*, 1508.
[30] D. Zhang, W. Liu, L. Tang, K. Zhou, H. Luo, *Appl. Phys. Lett.* **2017**, *110*, 133902.
[31] R. S. Friedlander, H. Vlamakis, P. Kim, M. Khan, R. Kolter, J. Aizenberg, *Proc. Natl. Acad. Sci. USA* **2013**, *110*, 5624.
[32] M. Cloutier, D. Mantovani, F. Rosei, *Trends Biotechnol.* **2015**, *33*, 637.
[33] K. W. Kolewe, J. Zhu, N. R. Mako, S. S. Nonnenmann, J. D. Schiffman, *ACS Appl. Mater. Interfaces* **2018**, *10*, 2275.
[34] A. Razatos, Y.-L. Ong, M. M. Sharma, G. Georgiou, *Proc. Natl. Acad. Sci. USA* **1998**, *95*, 11059.
[35] A. Labernadie, C. Thibault, C. Vieu, I. Maridonneau-Parini, G. M. Charrière, *Proc. Natl. Acad. Sci. U.S.A.* **2010**, *107*, 21016.
[36] D. J. Müller, Y. F. Dufrêne, *Nat. Nanotechnol.* **2008**, *3*, 261.
[37] H. J. Busscher, H. van der Mei, *PLoS Pathog.* **2012**, *8*, e1002440.
[38] Y. Liu, J. Strauss, T. A. Camesano, *Biomaterials* **2008**, *29*, 4374.
[39] E. R. Rojas, G. Billings, P. D. Odermatt, G. K. Auer, L. Zhu, A. Miguel, F. Chang, D. B. Weibel, J. A. Theriot, K. C. Huang, *Nature* **2018**, *559*, 617.
[40] B. Bhushan, *Springer Handbook of Nanotechnology*, Springer, New York **2017**.
[41] M. A. A. Ayee, I. Levitan, *Curr. Top. Membr.* **2018**, *81*, 97.
[42] A. Tripathy, P. Sen, B. Su, W. H. Briscoe, *Adv. Colloid Interface Sci.* **2017**, *248*, 85.
[43] K. Nowlin, A. Boseman, A. Covell, D. LaJeunesse, *J R Soc Interface* **2015**, *12*, 20140999.
[44] H. Strahl, L. W. Hamoen, *Proc. Natl. Acad. Sci. USA* **2010**, *107*, 12281.
[45] B. E. Logan, *Nat. Rev. Microbiol.* **2009**, *7*, 375.
[46] G. Reguera, *Proc. Natl. Acad. Sci. USA* **2018**, *115*, 5632.
[47] F. Kracke, I. Vassilev, J. Krömer, *Front Microbiol* **2015**, *6*, 575.
[48] X. Zhao, K. Drlica, *Curr. Opin. Microbiol.* **2014**, *21*, 1.
[49] H. Van Acker, T. Coenye, *Trends Microbiol.* **2017**, *25*, 456.
[50] T. A. Taton, *Nature* **2001**, *412*, 491.
[51] S. F. Lamolle, M. Monjo, M. Rubert, H. J. Haugen, S. P. Lyngstadaas, J. E. Ellingsen, *Biomaterials* **2009**, *30*, 736.
[52] P. Schäfer, B. Fink, D. Sandow, A. Margull, I. Berger, L. Frommelt, *Clin. Infect. Dis.* **2008**, *47*, 1403.
[53] W. Guan, L. Tan, X. Liu, Z. Cui, Y. Zheng, K. W. K. Yeung, D. Zheng, Y. Liang, Z. Li, S. Zhu, *Adv. Mater.* **2021**, *33*, 2006047.
[54] A. G. Gristina, M. Oga, L. X. Webb, C. D. Hobgood, *Science* **1985**, *228*, 990.
[55] J. Liu, D. A. Sonshine, S. Shervani, R. H. Hurt, *ACS Nano* **2010**, *4*, 6903.
[56] G. Wang, K. Tang, Z. Meng, P. Liu, S. Mo, B. Mehrjou, H. Wang, X. Liu, Z. Wu, P. K. Chu, *Adv. Mater.* **2020**, *32*, 2003616.
[57] M. I. Ishak, X. Liu, J. Jenkins, A. H. Nobbs, B. Su, *Coatings* **2020**, *10*, 756.
[58] K. Su, L. Tan, X. Liu, Z. Cui, Y. Zheng, B. Li, Y. Han, Z. Li, S. Zhu, Y. Liang, *ACS Nano* **2020**, *14*, 2077.
[59] S. Sahoo, K. K. Rao, G. Suraishkumar, *Biotechnol. Bioeng.* **2006**, *94*, 118.
[60] X. Li, K.-H. Tsui, J. K. Tsoi, D. W. Green, X.-z. Jin, Y. Q. Deng, Y. M. Zhu, X. G. Li, Z. Fan, G. S.-p. Cheung, *Nanoscale* **2020**, *12*, 18864.
[61] T. Y. Ma, J. L. Cao, M. Jaroniec, S. Z. Qiao, *Angew. Chem., Int. Ed.* **2016**, *128*, 1150.

© 2023 Wiley-VCH GmbH

ADVANCED MATERIALS

Supporting Information

for *Adv. Mater.,* DOI: 10.1002/adma.202212315

Quantifiable Relationship Between Antibacterial Efficacy and Electro–Mechanical Intervention on Nanowire Arrays

Guomin Wang, Kaiwei Tang,* Wenjuan Jiang, Qing Liao, Yong Li, Pei Liu, Yuzheng Wu, Mengting Liu, Huaiyu Wang, Bin Li, Jianzhong Du,* and Paul K. Chu**

Supporting Information

Quantifiable Relationship Between Antibacterial Efficacy and Electro–Mechanical Intervention on Nanowire Arrays

Guomin Wang, Kaiwei Tang,* Wenjuan Jiang, Qing Liao, Yong Li, Pei Liu, Yuzheng Wu, Mengting Liu, Huaiyu Wang, Bin Li, Jianzhong Du,* Paul K. Chu**

Dr. G. Wang, Prof. J. Du
Department of Orthopedics, Shanghai Tenth People's Hospital, School of Medicine, Tongji University, Shanghai, 200072 China
E-mail: gwang@tongji.edu.cn (G.M. Wang); jzdu@tongji.edu.cn (J.Z. Du)

Dr. G. Wang, Dr. K. Tang, P. Liu, Y. Wu, Prof. P. K. Chu
Department of Physics, Department of Materials Science and Engineering, and Department of Biomedical Engineering, City University of Hong Kong, Tat Chee Avenue, Kowloon, Hong Kong, China
E-mail: tangkaiwei@xtu.edu.cn (K.W. Tang); paul.chu@cityu.edu.hk (P.K. Chu)

Dr. K. Tang
School of Materials Science and Engineering, Xiangtan University, Xiangtan 411105, Hunan, China

Dr. W. Jiang
College of Pharmacy, Western University of Health Sciences, 309 E. Second St, Pomona, CA 91766, USA

Q. Liao, Prof. H. Wang
Center for Human Tissues and Organs Degeneration, Shenzhen Institutes of Advanced Technology, Chinese Academy of Sciences, Shenzhen 518055, China

Dr. Y. Li
Department of Applied Biology and Chemical Technology and the State Key Laboratory of Chemical Biology and Drug Discovery, The Hong Kong Polytechnic University, Hung Hom, Kowloon, Hong Kong, China

Dr. M. Liu
USC Stevens Neuroimaging and Informatics Institute, Keck School of Medicine of USC, University of Southern California, Los Angeles, CA 90033, USA

Prof. B. Li
Department of Orthopaedic Surgery, Orthopaedic Institute, First Affiliated Hospital, Medical College, Soochow University, Suzhou Jiangsu, 215007, China

Prof. J. Du
Department of Polymeric Materials, School of Materials Science and Engineering, Tongji University, 4800 Caoan Road, Shanghai 201804, China

Keywords: electro–mechanical forces, antibacterial surface, biomechanical, bioelectrical, molecular dynamics

Supplementary Figures

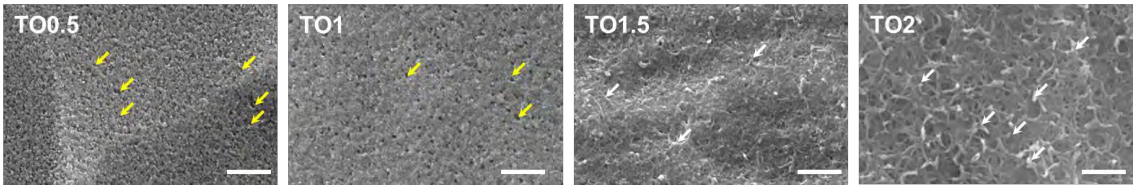

Supplementary Figure 1. Changes in the surface morphology during the first 2 h. Some of the nanopores and nanowires are indicated by the yellow and white arrows and show that the process starts with erosion and dissolution in the first hour. Afterwards, nucleation occurs and gradually becomes dominant. After 2 hours, nanowires are formed on the surface (scale bars = 500 nm).

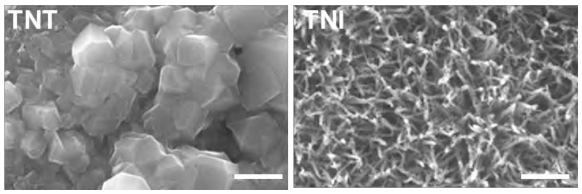

Supplementary Figure 2. Top views of TNT and TNI(scale bars = 500 nm).

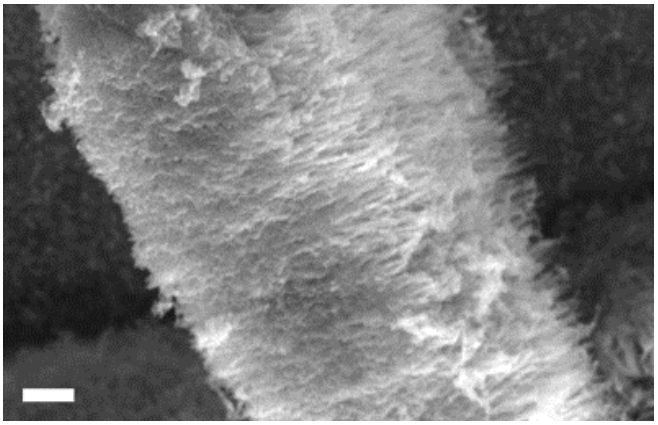

Supplementary Figure 3. Cross-section of the nanowires after hydrothermal reaction for 24 h (TOV24). The nanowires are vertically aligned with an average length of 2 μm (scale bar = 500 nm).

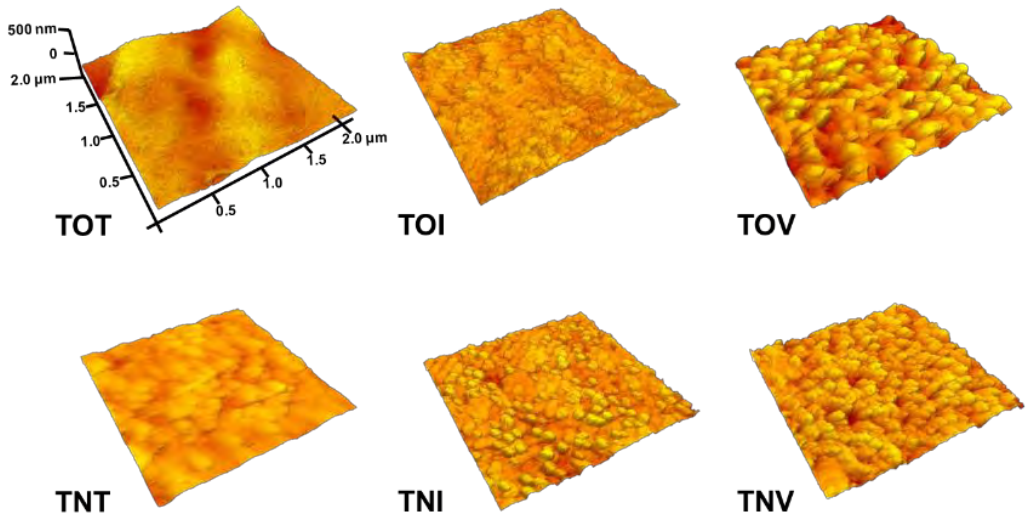

Supplementary Figure 4. 3D surface morphology of the samples revealed by AFM using the tapping mode. TOT and TNT show tiled nanowires on the substrate. The nanowires on TOI and TNI grow obliquely at an angle (40°- 60°) and those on TOV and TNV are almost perpendicular to the substrate.

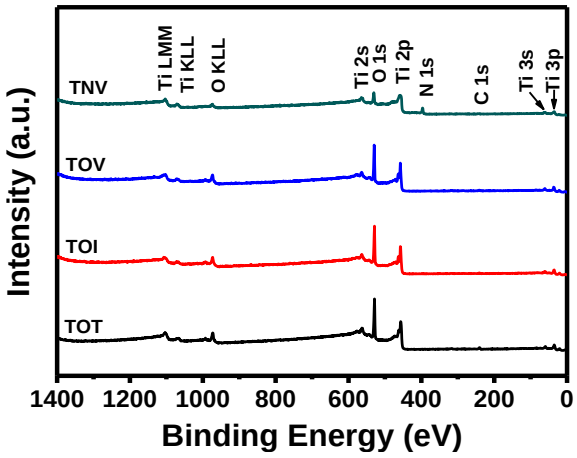

Supplementary Figure 5. Survey XPS spectra of the samples disclosing Ti-O in TOT, TOI and TOV as well as transformation from T-O to T-N on TNV.

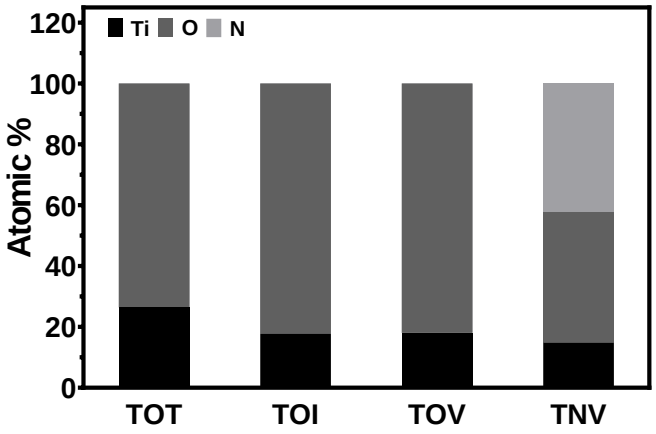

Supplementary Figure 6. Semi-quantitative analysis of Ti, O, and N by EDS. The spectrum of TO is dominated by Ti and O and after addition of N, TNV is doped with nitrogen.

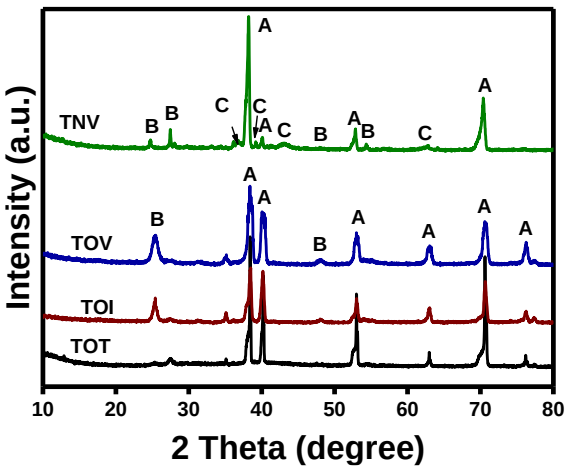

Supplementary Figure 7. XRD patterns of different samples showing peaks of A-Ti, B-rutile TiO_2, and C-TiN.

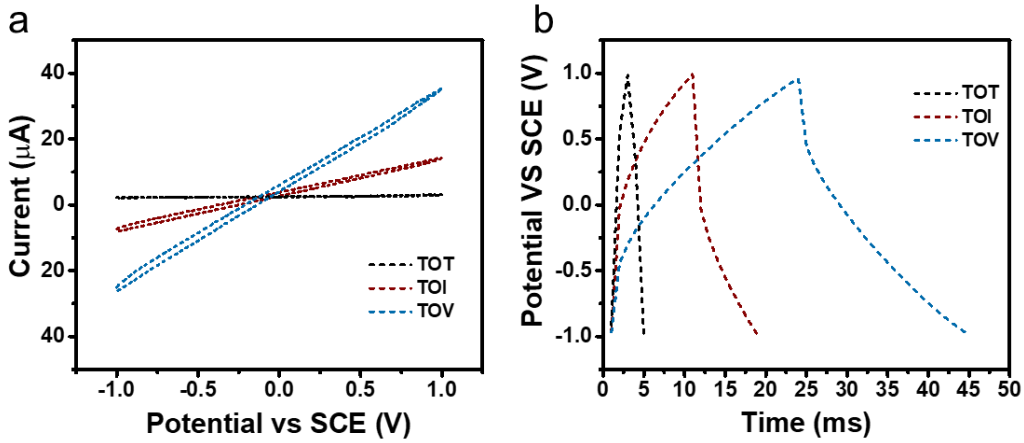

Supplementary Figure 8. Electrochemical properties of TO samples: (a) Cyclic voltammetry (CV) curves acquired at 100 mV s^{-1} from the second cycle; (b) Galvanostatic charging-discharging curves acquired at 2.5 mA cm^{-2} from the second cycle. As shown in Supplementary Figure 8a, TOT, TOI, and TOV do not show an obvious electrochemical double-layer (EDL). TN performs better than TO with TNV showing the longest charging and discharging time (Figure 2b and Supplementary Figure 8b).

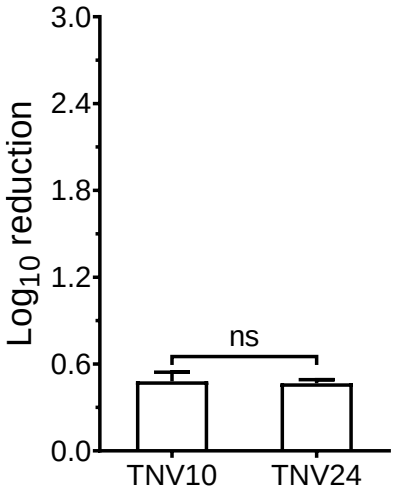

Supplementary Figure 9. Antibacterial efficiency of nanowires with different lengths against *E. coli*. When the reaction time is increased from 10 h to 24 h, the nanowires grow from 1 μm to nearly 2 μm. However, this does not contribute significantly to the antibacterial efficiency.

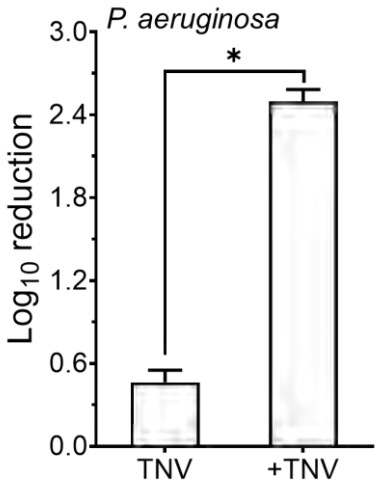

Supplementary Figure 10. Antibacterial efficiency of the samples against *P. aeruginosa* with * denoting significant difference between groups ($P < 0.05$).

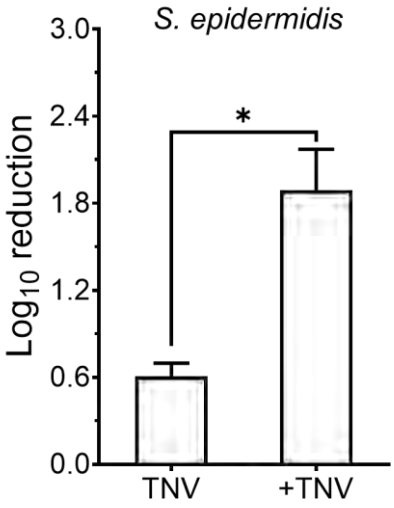

Supplementary Figure 11. Antibacterial efficiency of the samples against *S. epidermidis* with * denoting significant difference between groups ($P < 0.05$).

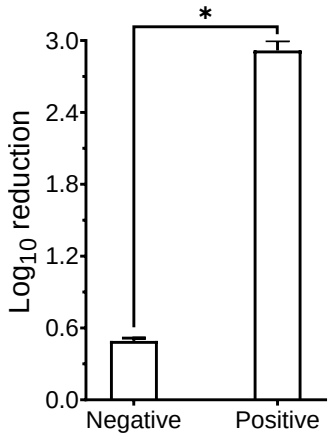

Supplementary Figure 12. Antibacterial properties of TNV after positive or negative charging with * denoting significant difference between groups ($P < 0.05$).

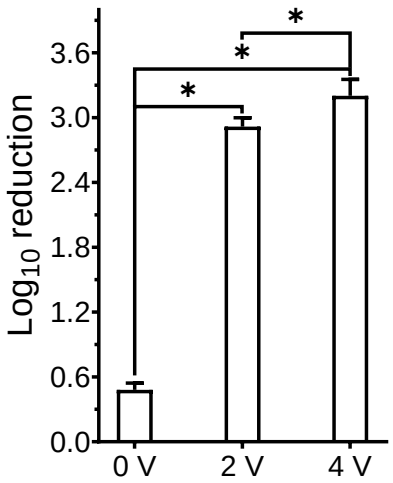

Supplementary Figure 13. Antibacterial efficiency of charged TNV for different charging voltages with * denoting significant difference between groups ($P < 0.05$).

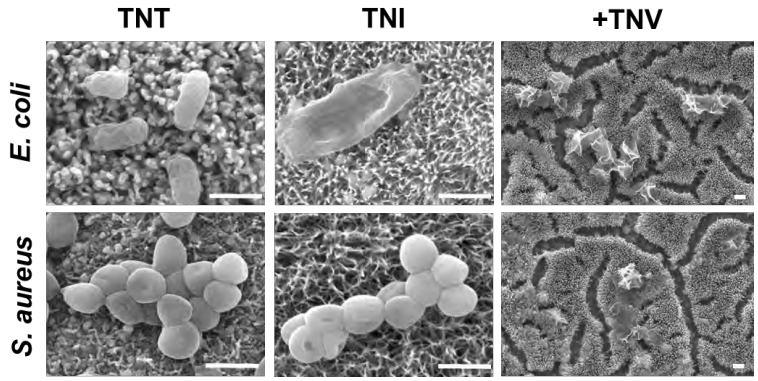

Supplementary Figure 14. Morphology of *E. coli* and *S. aureus* on TNT, TNI and +TNV (with lower magnification) after the treatment (scale bars = 1 μm). The sparsely distributed and tiled nanowires on TNT hinder proliferation of bacteria and some of them are slightly shriveled. The protruding nanowires on TNI lead the partial membrane collapse. Bacteria wreckages are sparsely observed from the surface of +TNV.

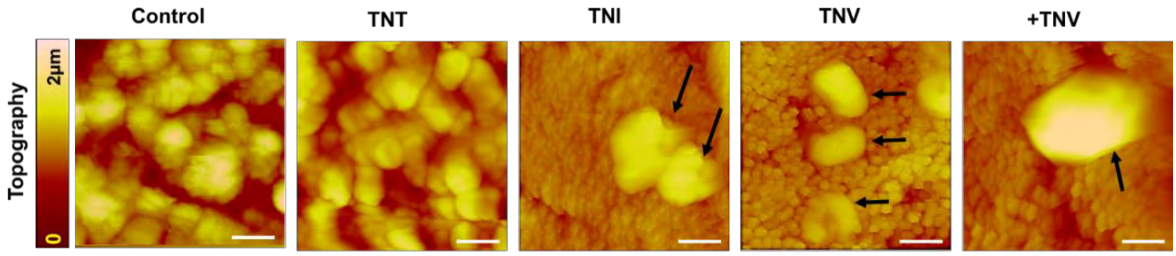

Supplementary Figure 15. Topographical maps of bacteria cultivated on different samples in an area of 5 μm × 5 μm (scale bars = 1 μm). The biophysical changes during bacteria-materials interactions provide clues to the bacteria killing process. The surface topography and potential maps of the samples in a 5 μm × 5 μm area are scanned by AFM using the tapping mode. The 3D surface topographical images supply information about not only the bacteria location (2D image), but also the height from the surface (brightness, Supplementary Figure 15). The bacteria distribution resembles that disclosed by SEM. The bacteria density on the control and TNT is so large that the substrate can hardly be recognized. In contrast, few bacteria adhere onto the surface of TNI, TNV and +TNV and morphological disruptions are detected (black arrows in Supplementary Figure 15). Notably, the bacteria on +TNV are mostly deformed indicating the harshest environment after charging.

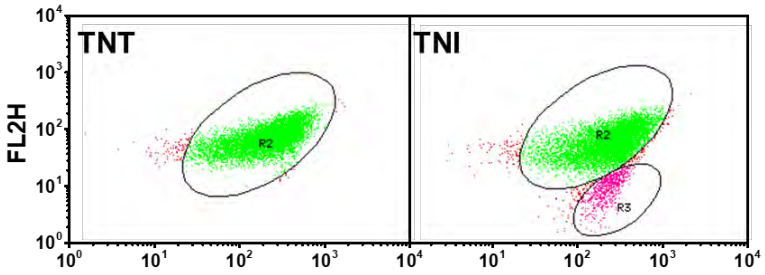

Supplementary Figure 16. Membrane potential dots of bacteria determined by flow cytometry. As shown in Figure 5a and Supplementary Figure 16, the membrane potentials on the control and TNT are at the same level. The bacteria are distributed in two regions on TNI and TNV groups (R2 and R3). The membrane potential on R2 is similar to that of the control, but that on R3 decreases significantly, suggesting that TNI and TNV can only disrupt the bacteria upon direct contact while those in the further vicinity are not affected.

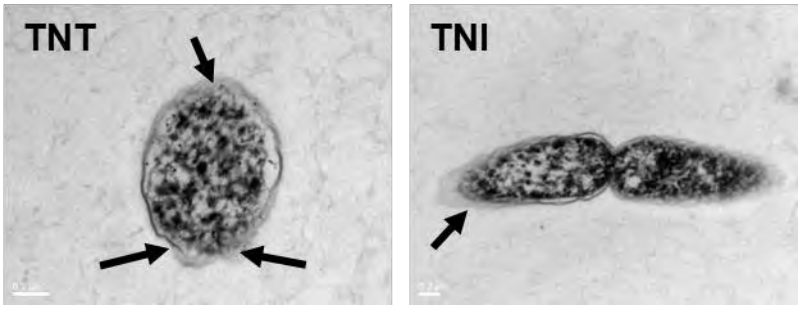

Supplementary Figure 17. TEM images of bacteria on TNT and TNI (scale bars = 200 nm).

The biochemical changes from electrochemical interactions are further examined by TEM on the sliced bacteria (Figure 5c and Supplementary Figure 17). The bacteria experience stronger membrane disruption in the order of TNT, TNI, TNV and +TNV (black arrows).

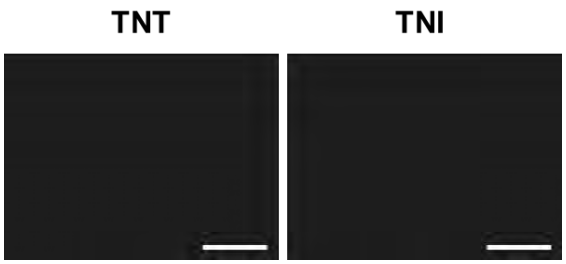

Supplementary Figure 18. Absolutely negative fluorescent staining signal of intracellular ROS on TNT and TNI (scale bars = 50 μm). The TNT, TNI, and TNV groups show a similar behavior as the negative control group with no intracellular ROS spot and +TNV is similar to the positive group exhibiting significant green spots.

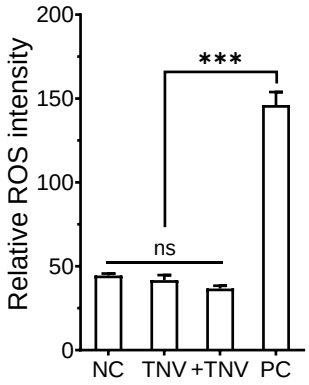

Supplementary Figure 19. Extracellular ROS intensities of different groups (NC = negative control and PC = positive control; *** denotes $P < 0.001$).

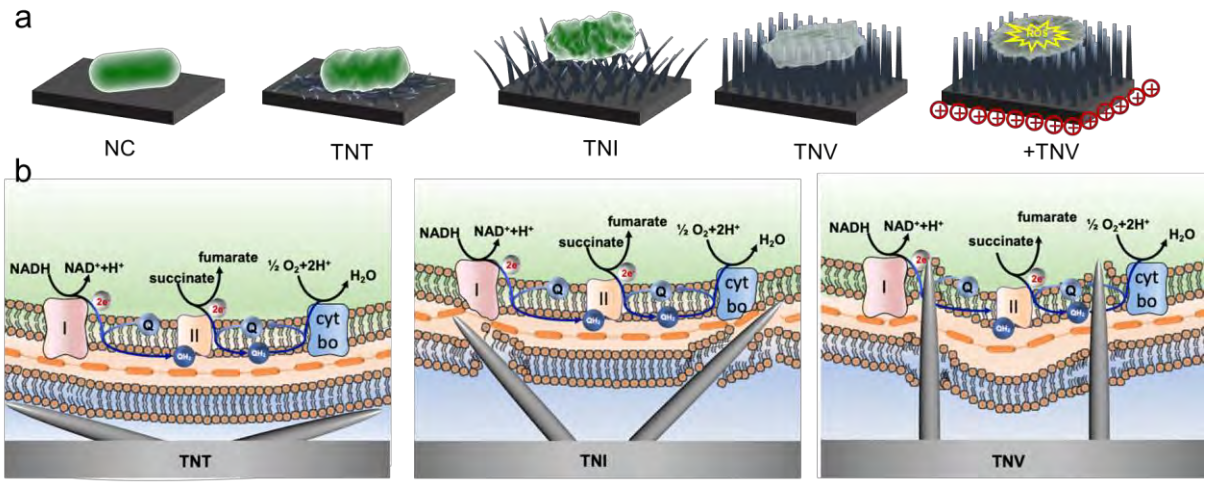

Supplementary Figure 20. Schematic diagrams showing how bacteria are affected on different surfaces. When bacteria are in contact with nanowires, mechanical disruption takes place and the vertical nanowires exert higher tension than the titled or the inclined ones as shown by the TNT, TNI and TNV groups. The gradually increasing membrane disruption corresponds to the antibacterial results (Fig. 3), AFM assessment (Fig. 4d), and membrane potentials (Fig. 5a).

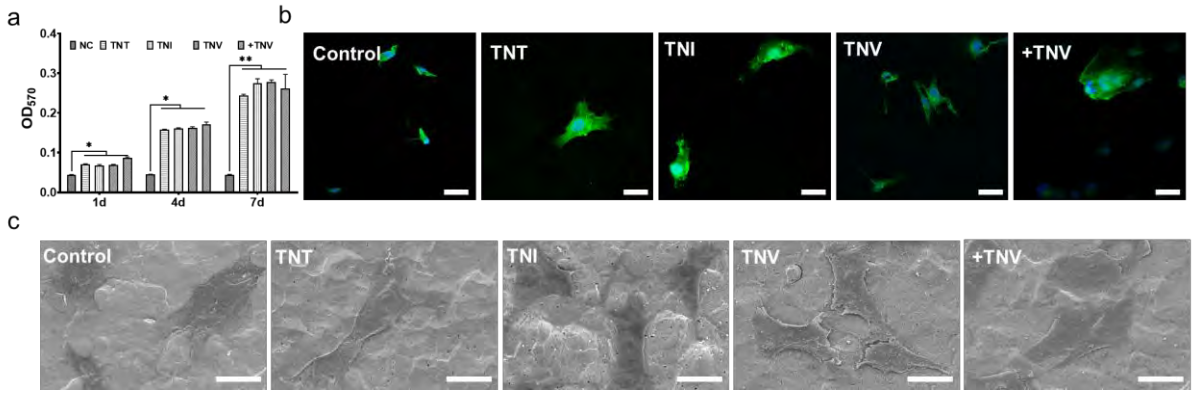

Supplementary Figure 21. *In vitro* biocompatibility assessment: (a) Quantitative determination of the cell viability at time points of 1 day, 4 days, and 7 days with * and ** denoting $P < 0.05$ and $P < 0.01$ compared to the control group, respectively; (b) Fluorescent images depicting the cytoskeleton of the osteoblasts cultivated on the different samples for 24 h (scale bars = 25 μm); (c) SEM images of the osteoblasts cultivated on different samples (scale bars = 25 μm). +TNV fares the best in the antibacterial test and the preliminary *in vitro* cell experiments provide the positive signal that none of the TN samples will do harm with regard to adherence and proliferation of osteoblasts and even foster the growth of osteoblasts as indicated by MTT (Supplementary Figure 21a). The cytoskeleton of the osteoblasts after cultivation for 24 h is observed after fluorescent staining (Supplementary Figure 21b). The osteoblasts in the four TN groups adhere onto the substrate and proliferate well showing spreading filopodia in a larger area than the control. The magnified SEM image is consistent (Supplementary Figure 21c). Comparing the charged and uncharged groups, no significant difference is found illustrating that the nanostructure but not the positive charge, boosts the growth of osteoblasts.

Supplementary Table 1. Density of the nanofeatures and angles between the substrate and nanowires on the different samples

Samples	Density of nanofeatures (μm)	Angles between substrate and nanowires
TOT	9.3	0
TOI	22	40°-50°
TOV	32.7	80°-90°
TNT	0	/
TNI	23.3	40°-50°
TNV	36	80°-90°

Supplementary Table 2. Antibacterial rates of different samples shown in Fig. 3 in the main text

	Log10 reduction	
	E. coli	S. aureus
TOT	0.22±0.01	0.22±0.06
TOI	0.36±0.05	0.31±0.05
TOV	0.62±0.06	0.4±+0.10
TNV	0.49±0.04	0.46±0.15
+TOV	0.52±0.07	0.37±0.03
+TNV	2.92±0.07	1.91±0.29

Supplementary Table 3. Details of the simulated bacteria membrane and titania nanowires

Systems	Rutile (101)	POPG	POPE	TIP3	POT	CLA	Water/lipid ratio
Num of mol.	1	84	252	82590	276	321	245.8

Legends of Supplementary Videos 1 to 3

Supplementary Video 1. Dynamic simulation demonstrating the approaching and interacting processes between the bilayer and nanowire without voltage.

Supplementary Video 2. Dynamic simulation demonstrating the approaching and interacting processes between the bilayer and nanowire at a voltage of 20 mV.

Supplementary Video 3. Dynamic simulation demonstrating the approaching and interacting processes between the bilayer and nanowire at a voltage of 200 mV.

Experimental Section

Preparation of titanium oxide/nitride nanowires

Pure titanium plates with dimensions of 10 × 10 × 1 mm were selected as the substrates. The titanium oxide (TO) nanowires were synthesized by a wet oxidation process. The melamine solution (0.004 g mL^{-1}), hydrogen peroxide (30 wt%), and nitric acid (65 wt%) with a volume ratio of 25:25:1 were mixed ultrasonically. Afterwards, clean titanium plates were put horizontally or vertically into the solution (ratio of titanium plates to the solution is 1 cm^2 to 1.0 mL of the solution). The synthesis was carried out in the blast oven at 80 °C for 0-10 h and tiled, inclined, and vertical TO nanowires were formed on the substrate by adjusting the initial orientation and reaction time. The samples were labeled TOT, TOI, and TOV, respectively. After the reaction, the samples were washed with deionized water and dried at room temperature. TO was then annealed in a tube furnace at 850 °C for 1.5 h in air atmosphere for stabilization. The unannealed TO was treated under nitrogen in a tubular furnace. The sample was placed on a corundum crucible in the tubular furnace and the corundum crucible contained 5.0 g of urea and placed at a distance of 3 cm in the upwind direction. The nitrogen treatment was carried out at 850 °C for 1.5 h under flowing nitrogen (50 sccm) at a heating rate of 5 °C min^{-1}. The titanium nitride (TN) samples were obtained after cooling in the furnace and designated as TNT, TNI, and TNV, respectively.

Materials and morphological characterization

The morphology of the samples was examined by scanning electron microscopy (SEM) (XL30, ESEM-FEG, Philips, Holland) and atomic force microscopy (AFM) (Veeco MultimodeV). The chemical states were determined by XPS (K-Alpha, Thermo Fisher

Scientific, USA) with Al K_α radiation referenced to the Ar 2*p* peak at 242.4 eV. Elemental depth profiling was performed by XPS using an approximate sputtering rate of 31.5 nm min^{-1}. The composition and crystallinity of the samples were determined by XRD (SRD-D2 Phaser, Bruker, Germany) with Cu K_α irradiation (λ = 1.54184 Å) at 30 kV and 10 mA and Raman scattering (Horiba Jobin-Yvon Lab Ram HR VIS high-resolution confocal Raman microscope with a 633 nm laser as the excitation source). High-resolution images were acquired at 200 kV by field-emission STEM (JEOL JEM-2010F) to reveal the lattices.

Electrochemical characterization

The electrochemical properties of the samples were determined using a three-electrode system on an electrochemical workstation (CHI660, Chenhua, China) in LB to mimic the bacterial growth environment. The sample (1 cm × 1 cm), platinum wire, and saturated calomel electrode (SCE) served as the working electrode, counter electrode, and reference electrode, respectively. Cyclic voltammetry (CV) was carried out from −1 to 1 V at a scanning rate of 100 mV s^{-1} and galvanostatic charge-discharge (GCD) tests were performed at a constant charging current of 2.5 mA cm^{-2}. The capacitance density was determined by the following equation:

$$C = i \times \Delta t / \Delta V,$$

where i is the current density, Δt is the discharging time and ΔV is the potential window. One-time discharging curve of the charged (charged to 1 V) sample was recorded for 4 h with the working electrode and counter electrode separated by 1 cm. The discharging capacities of the charged samples were calculated by the line integral.

Antibacterial analysis

The antibacterial activity of the sterilized samples was assessed with Gram-positive (*Staphylococcus aureus*, 29213; *Staphylococcus epidermidis*, pAO1) and Gram-negative (*Escherichia coli*, ATCC 25922; *P. aeruginosa*, clinical isolate) bacteria. In brief, the pure bacteria in LB were cultivated overnight in a rotating shaker at 37 °C and cultivated to a concentration of 1×10^9 CFU mL^{-1} (OD_{600} = 0.2 for *S. aureus* and OD_{600} = 0.2 for *E. coli*). The bacteria solution was diluted for the antibacterial test. The samples were immersed in 75% alcohol for 30 min for sterilization and dried in nitrogen before they were prepared on the anode of the reaction kettle. After 6 h, the adhered bacteria were detached from the surface with 900 μL of the saline solution, diluted to the proper concentration, spread on a solid agar plate, and cultivated for another 18 h to count the CFU. To determine the antibacterial efficiency after electrochemical interactions, the samples were charged for 20 min immediately before the bacteria cultivation. The antibacterial rate was determined by the following formulas: Antibacterial rate = $(1 - CFU_{experimental\ group} / CFU_{control\ group}) \times 100\%$; Log_{10} reduction = $-\log_{10}$ (1-antibacterial rate).

After bacterial cultivation for different durations, the samples were treated with 2.5% glutaraldehyde overnight and dehydrated with a series of gradient alcohol solutions (30, 50, 75, 90, 95, and 100%) for 10 min sequentially before drying at room temperature. The integrity and morphological changes of the bacteria were observed by SEM.

Live/dead and intracellular ROS staining

The bacteria on the samples were stained by the LIVE/DEAD® *Bac*Light™ Bacterial Viability Kit (L-7012, Molecular Probes, Thermo Fisher Scientific, USA) after cultivation. The

live bacteria were stained green and dead bacteria were stained red. 15 min after staining, the samples with bacteria were gently washed with PBS to remove the excess dye and put on a glass slide for observation under an inverted fluorescent microscope (BM-20AYC, BM) with 488/520 nm and 488/630 nm as the excitation/emission wavelengths for green and red fluorescence, respectively.

After cultured for 1 h, samples with bacteria were washed with PBS three times and stained with 2', 7'-dichlorodihydrofluorescein diacetate (DCFDA, Beyotime, China) for 15 min in darkness. The excess dye was removed by PBS and the samples were observed under an inverted fluorescent microscope with 488 nm as the excitation wavelength and 520 nm as the emission wavelength.

Bacterial morphology observed by SEM and inner structure of the bacteria examined by TEM

After incubation for 24 h, the specimens were treated ultrasonically for 5 min in PBS to dislodge bacteria from the sample surface. The solution was centrifuged for 5 min (4,000 × g) to collect the bacteria from the bottom. Prior to SEM observation, the samples were fixed with 2.5% glutaraldehyde, washed by PBS and sequentially dehydrated with alcohol (10%, 30%, 50%, 70%, 90%, 100%), dried in air, and coated with a thin gold layer to reduce charging. Before performing TEM, the bacteria were fixed successively with 2.5% glutaraldehyde and 1% OsO_4 at room temperature overnight. After washing with PBS and dehydration with alcohol and acetone with gradient concentrations, the samples were embedded in Spurr's resin (Spurr Embedding Kit, Spurr, USA) before slicing into sections (<100 nm thick) with a glass knife and staining with uranylacetate. The stained samples were placed on a copper wire mesh

and examined by TEM (TecnaiG^{2}12 BioTWIN, FEI company, USA) at 120 kV.

Membrane potential determination

The potential of the bacteria membrane was evaluated by a membrane potential kit (B34950, Invitrogen, USA) with the bacteria treated with CCCP serving as the positive control. The bacteria depolarization level was qualitatively characterized as the dots in flow cytometer and quantitatively calculated as the red/green fluorescence ratio. More information about the procedures can be found elsewhere [1].

Nanomechanical analysis by AFM

After the antibacterial evaluation, the samples with bacteria (bacteria on the Ti plate as control) were analyzed by AFM (Veeco, CA, USA). Nanoindentation was applied in the nanomechanical measurement. In details, the spring constant (k) of the cantilever tip with the diamond surface (supposed to be absolutely hard) was tested as the standard sample. The force on the tip was calculated by the equation: Hooke's Law $F = -k \times x$. The cantilevers were pyramidal probes with a spring constant of 0.05 N m^{-1} and the front and back angle was 35° (Veeco Instruments Ltd., Cambridge, UK). AFM was conducted in the tapping mode with the cantilever moved across the surface at 1 Hz in an area of 5 μm × 5 μm. The 3D topographical images were reconstructed according to the survey maps. Afterwards, the AFM tip was placed on the bacteria and force measurements were performed to obtain the force-distance curves, where the distance traveled by the tip was plotted against the deflection of the cantilever. During the movement before contact, no force was detected. At the beginning of the contact, the tip was attracted by the surface to produce a non-linear curve, from which the adhesion force of the membrane was derived. When the tip traveled further, the attraction was be

replaced by repelling force and a linear curve was obtained. Since a harder surface generated a larger force with the same position variation, the slope of the linear part could be used to compare the hardness of the surface since a hard sample produced a steeper curve than a soft one. More detailed explanation is available in previous paper.[2-3]

Molecular dynamic simulation

The titania force field was initially developed by the Lyubartsev group [4]. M. Schneemilch and N. Quirke derived the force field parameters from the electron densities generated by DFT simulations, which could reproduce the DFT surface water density profiles and empirically determined the water adsorption enthalpies [5]. In our simulation, we chose the rutile 101 surface titania nanoparticles from Schneemilch's paper, which was cut to a 50Å×20Å ×90Å nanowire shape for simplicity and with a charge of +129 on the top and bottom surfaces. The force field parameters for the titania rutile 101 surface were also modified accordingly.

In order to mimic the bilayer performance for the bacteria, the membrane components of 1-palmitoyl-2-oleoyl-sn-glycero-3-phosphoethanolamine (POPE, neutral lipid) and 1-palmitoyl-2-oleoyl-sn-glycero-3-phospho-(1'-rac-glycerol) (POPG, -1 charged lipid) with a ratio of 3:1 were selected for each leaflet. The main component of the bacteria was POPE with about 25% charged lipids chosen as POPG.[6] The POPE and POPG lipids were modeled using the CHARMM36 lipids force fields and CHARMM TIP3P water model [7]. The details about the simulation systems are shown in Supplementary Table 1. The bilayer and nanowire were solvated in 150 mM KCl solution and the simulation was performed with the GROMACS 2016.4 engine using a 1 fs time step. The overall workflow of the simulation included initial construction of the energy minimization, isothermal-isochoric (NVT) and isothermal-isobaric (NPT) equilibration runs, and NPT production runs. NVT simulation was carried out for 25 ns

at 310.15 K and NPT equilibration simulation proceeded for 5 ns, followed by 50 ns NPT production run without a voltage. The electrostatic interactions were calculated by Particle Mesh Ewald (PME) summation [8]. A cutoff of 1.2 nm was used to calculate both the short-range electrostatic and van der Waals interaction with the Potential-shift-Verlet algorithm applied to smoothly shift beyond the cutoff. The long-range electrostatic interaction was calculated by the reaction-field algorithm implemented in GROMACS. The neighbor list was updated every 20 steps using a neighbor list cutoff equal to 1.0 nm for van der Waals. The temperature of each group (protein, membrane, titania, ions, and water) was kept constant by the Nose-hoover algorithm with a 5 ps time constant. The pressure was maintained at 1 bar using a semi-isotropic Berendsen barostat with a relaxation time constant of 10 ps and the three-dimensional periodical boundary conditions (PBC) were adopted. To identify the interactions between the bilayer membrane and titania nanowires under a voltage, voltage simulation of 20 mV and 200 mV was conducted after 50 ns non-voltage run. The voltage in GROMACS 2016.4 was set through E-z [9] and for the 20 mV and 200 mV voltages, the simulation was carried out for 30 ns and 5 ns, respectively.

The area compressibility K_A is an important mechanical property of a bilayer that quantifies the response of membrane area to tension. In the symmetric bilayer with minimum undulations (the difference in projected areas and local areas is negligible), the area compressibility K_A can be evaluated from the mean square fluctuation of the total area of the bilayer [10] or the probability distribution of the area change around the mean [11]. Here, K_A was calculated based on local thermal fluctuations of the leaflet thickness. In this approach, each leaflet was viewed as a collection of more than one parallel elastic block with the same average area but different instantaneous areas. The interleaflet coupling was shown to be equivalent to the variance of the bilayer area A ($\sigma^2(A)$) and the local area fluctuation was then converted to the local thickness fluctuation assuming volume conservation. The curvature was also closely

related to the mechanical property of the bilayer and the Gaussian curvature after simulation was calculated according to a previous study [12].

In vitro biocompatibility evaluation

The MC3T3-E1 osteoblasts obtained from the cell bank of the Chinese Academy of Sciences were used to study the biocompatibility of the samples *in vitro*. The cells were nurtured in the culture medium containing the Dulbecco's modified eagle medium (DMEM) and 10% fetal bovine serum (FBS) and incubated in a humidified atmosphere of 5% CO_2 at 37 °C with the medium refreshed every other day. The cells in the logarithmic growth phase were harvested, centrifuged for 5 min, and diluted to 2×10^4 cells mL^{-1}. The samples were disinfected and 1 mL of the cell solution was seeded on a 24-well plate. The MTT assay was employed to evaluate the cell viability. After cultivation for 1 day, 4 days, and 7 days, the medium on the 24-well plate was removed and 1 mL of the MTT solution was added to each well. After further incubation for 4 h, the MTT solution was replaced with the DMSO solution to dissolve the formazan crystals. Subsequently, 100 μL of the solution was transferred to a 96-well plate and the optical density at 570 nm was measured on a multimode reader (EON, BioTek, USA) with DMSO as the negative control. To assess adhesion, the cells were rinsed with PBS twice, fixed with 4% paraformaldehyde, permeabilized with 0.2% Triton X-100 (Sigma, USA), stained with phalloidin-fluorescein isothiocyanate (Sigma, USA) for 60 min, and then stained with 4',6-diamidino-2-phenylindole (DAPI, Sigma, USA) for 5 min. The samples were observed under an inverted microscope (20AYC-BM, BM). The samples with cells were also fixed and examined by SEM to evaluate the morphology of the osteoblasts.

***In vivo* assessment of the antibacterial efficacy, anti-inflammatory effects, and biocompatibility**

The male and 12-week-old SD rats (200-300g) maintained in the animal room under specific pathogen-free (SPF) conditions were used in the *in vivo* assessment. Before surgery, the animals were housed for 1 week for acclimatization. All the animal experiments were carried out under sterile conditions and approved by the Ethics Committee for Animal Research, Shenzhen Institutes of Advanced Technology, Chinese Academy of Sciences. They were anesthetized with pentobarbital sodium (45 mg kg^{-1}) *via* intraperitoneal injection before the dorsal hair was shaved from a 3 cm × 5 cm area and sterilized with povidone iodine. After incising the skin layer-by-layer parallel to the spine, the samples with a size of 10 mm × 10 mm × 1 mm (Control, TOV, TNV, +TOV, +TNV) were implanted into the subcutaneous soft tissue. The skin incisions were sutured before *S. aureus* 100 μL of PBS (10^7 CFU mL^{-1}) were injected around the implant. The animals were individually housed in cages for healing. The inflammatory response was examined daily and after 5 and 10 days. Afterwards, the rats were euthanized and the implants were collected, immersed in PBS, and shaken for 2 min on a vortex shaker to count the implant-related CFU. Meanwhile, the surrounding soft tissues were immersed in PBS and homogenized (Scientz-IID, Ningbo, Zhejiang, China) for CFU counting. In the histological observation, other parts of the soft tissues were fixed with 10% buffered formalin, washed with PBS, dehydrated in gradient alcohol, embedded in the paraffin, and sectioned. The sections were deparaffinized and stained with H&E and Gram stain before observation by optical microscopy. The infection and inflammation states were evaluated by comparing the distributions of bacteria and lymphocytes, respectively.

Statistical analysis

The data were presented as mean ± standard deviation (SD, n = 3). The data were evaluated by the *t*-test and Tukey test in ANOVA with the software of OriginPro 2016. Differences of $P < 0.05$ and $P < 0.01$ were considered significant and highly significant, respectively.

Supplementary References

[1] D. J. Novo, N. G. Perlmutter, R. H. Hunt, H. M. Shapiro, *Antimicrob. Agents Chemother.* **2000**, *44*, 827.

[2] C. Roduit, S. Sekatski, G. Dietler, S. Catsicas, F. Lafont, S. Kasas, *Biophys. J.* **2009**, *97*, 674.

[3] C. Rotsch, K. Jacobson, M. Radmacher, *Proc. Natl. Acad. Sci. U S A* **1999**, *96*, 921.

[4] L. Agosta, E. G. Brandt, A. P. Lyubartsev, *J. Chem. Phys.* **2017**, *147*, 024704.

[5] M. Schneemilch, N. Quirke, *J. Chem. Phys.* **2019**, *151*, 134707.

[6] C. Sohlenkamp, O. Geiger, *FEMS Microbiol. Rev.* **2016**, *40*, 133.

[7] J. Klauda, R. Venable, J. Freites, *J. Phys. Chem. B* **2010**, *114*, 7830.

[8] U. Essman, L. Perera, M. Berkowitz, T. Darden, H. Lee, L. Pedersen, *J. Chem. Phys.* **1995**, *103*, 8577.

[9] C. Caleman, D. van der Spoel, *Angew. Chem. Int. Ed.* **2008**, *47*, 1417.

[10] S. E. Feller, R. W. Pastor, *J. Chem. Phys.* **1999**, *111*, 1281.

[11] M. Doktorova, M. V. LeVine, G. Khelashvili, H. Weinstein, *Biophys. J.* **2019**, *116*, 487.

[12] W. M. Botello-Smith, W. Jiang, H. Zhang, A. D. Ozkan, Y. C. Lin, C. N. Pham, J. J. Lacroix, Y. Luo, *Nat. Commun.* **2019**, *10*, 4503.